



ELSEVIER

Available online at www.sciencedirect.com

SCIENCE @ DIRECT®

Coastal Engineering 49 (2003) 155–183

**Coastal
Engineering**
An International Journal for Coastal,
Harbour and Offshore Engineers

www.elsevier.com/locate/coastaleng

Effect of externally generated turbulence on wave boundary layer

Jørgen Fredsøe, B. Mutlu Sumer*, Andrzej Kozakiewicz,
Lloyd H.C. Chua, Rolf Deigaard

*Coastal and River Engineering Section (formerly Department of Hydrodynamics and Water Resources, ISVA),
Technical University of Denmark, MEK, Building 115, DK-2800 Lyngby, Denmark*

Received 3 July 2002; accepted 2 May 2003

Abstract

This experimental study deals with the effect of externally generated turbulence on the oscillatory boundary layer to simulate the turbulence in the wave boundary layer (WBL) under broken waves in the swash zone. The subject has been investigated experimentally in a U-shaped, oscillating water tunnel with a smooth bottom. Turbulence was generated ‘externally’ as the flow in the oscillator was passed through a series of grids that extended from the cover of the water tunnel to about mid-depth. Two different types of grid porosities were used. Direct measurements of the bed shear stress and velocity measurements were carried out. For the velocity measurements, mean and turbulence properties were measured in both the streamwise direction and in the direction perpendicular to the bed. A supplementary measurement for the undisturbed (without grids) case was also carried out, for comparison with the grid results. The mean and turbulence quantities in the outer flow region are increased substantially with the introduction of the grids. It is shown that the externally generated turbulence is able to penetrate the bed boundary layer, resulting in an increase in the bed shear stress, and therefore the friction coefficient. Other features related to the bed shear stress, such as transition, the friction factor and phase lead, are discussed. The range of the Reynolds number studied is $Re = 1 \times 10^4 - 2 \times 10^6$.

© 2003 Elsevier B.V. All rights reserved.

Keywords: External turbulence; Grid-generated turbulence; Spilling breaker; Wave boundary layers

1. Introduction

In the natural environment, the wave boundary layer is very often subject to some momentum exchange process between itself and the flow in the outer fluid layer. This momentum exchange process is brought about by the presence of an externally generated turbulence field. A very strong candidate for production of external generated turbulence is the spilling breaker where turbulence is generated in the strongly sheared

flow beneath the surface roller. The turbulence decays and spreads downwards in a way that may resemble a wake (Peregrine and Svendsen, 1978). The sheared flow in the spilling breaker is associated with a strong near-surface shear stress, the magnitude of which is related to the rate of energy dissipation in the breaking/broken wave, see e.g. Fredsøe and Deigaard (1992). The near-surface shear stress corresponds to a forcing in the direction of the wave propagation. The mean shear stress decreases towards the bed; it is zero at a distance above the bed to attain a small negative value at the bed. This mean shear stress distribution determines the mean velocity distribution of the vertical

* Corresponding author. Fax: +45-45-932860.

E-mail address: sumer@isva.dtu.dk (B.M. Sumer).

circulation pattern in the surf zone with a relatively strong offshore directed undertow near the bed. In such a situation the externally generated turbulence field can penetrate the wave boundary layer. Obviously, when this happens, the characteristics of the wave boundary layer will change. An experimental investigation was therefore undertaken to investigate the effect of externally generated turbulence on the wave boundary layer. To the authors' knowledge, a study of this nature has not been undertaken before.

The characteristics of boundary layer is of large importance for sediment transport (Grant and Madsen, 1986) since the sediment has to be picked up from the bed by the turbulence in the boundary layer; features like turbulence characteristics and phases between the outer flow and boundary layer flow are necessary information for a correct description of the sediment transport pattern in the boundary layer.

In recent years, detailed field measurements have contributed to the understanding and quantification of the hydrodynamic processes in the surf zone. As shown by Feddersen et al. (1998), the longshore force balance in the surf zone involves mainly the gradient in the shear component of the wave radiation stress (the driving force) and the mean bed shear stress (the retarding force). The prediction of the friction coefficient related to the mean current in a surf zone is difficult (e.g. Feddersen and Guza, 2000), and it may

be improved when more details are known about the structure of the turbulence in the near-bed oscillatory boundary layer and the interaction with the turbulence generated by the wave breaking.

One problem encountered in the experimental investigation of the wave boundary layer (WBL) is that it is very thin, of the order of 0–5 cm. In the laboratory, it is usually difficult to get the boundary layer turbulent in an ordinary small wave flume. For this reason, the WBL is quite often studied in an oscillatory tunnel where much larger near-bed orbital velocities can be obtained. Examples of such tunnels are the Danish oscillating water tunnel (Lundgren and Sørensen, 1958), the Dutch one (see e.g. Ribberink and Alselaam, 1995), and the Japanese oscillating wind tunnel (Hino et al., 1983).

The problem when employing an oscillating tunnel is that one cannot produce a spilling breaker. So, an investigation of the boundary layer must be done either in a large-scale facility (like the Delft Hydraulics Delta Flume), or—as selected in the present work—in an oscillating water tunnel but in an artificial manner. In the present investigation, we have decided to employ the oscillating water tunnel to get Reynolds numbers high enough so that the field conditions can be attained. Furthermore, we have decided to create the external turbulence by introducing a series of vertical grids in the upper half of the tunnel (Figs. 1 and 2b–d). In

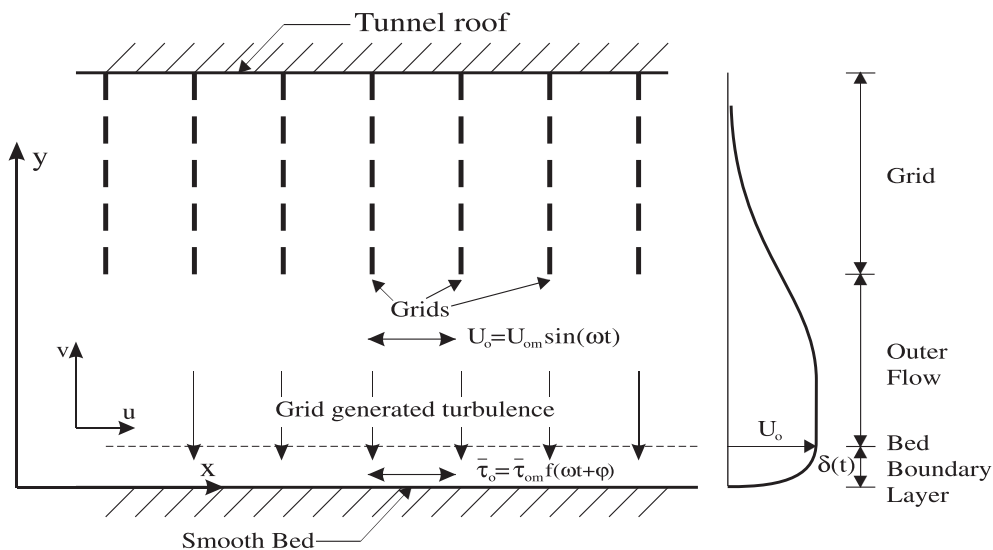


Fig. 1. Definition sketch.

this way, we can control the externally generated turbulence for instance by changing the size of the holes in the grids. Turbulence will be generated by the flow through the grid, and due to the flow resistance the mean velocity in the grid will be reduced relative to the free-stream velocity in the region between the grid and the bed. The velocity difference between the flow through the grid and the flow outside will cause a significant rate of production of turbulence in the almost uniform shear boundary layer formed along the lower edge of the grid. The length scale of the turbulence in this boundary layer is not restricted by the proximity of a wall and it will typically be much larger than the length scale of the turbulence generated in the oscillatory bed boundary layer. The outer turbulence, which spreads downwards to interact with the near-bed oscillatory boundary layer, will be a combination of the turbulence generated by flow through the grid and of the turbulence generated in the upper boundary layer. The thickness of this upper boundary layer is large as the turbulence spreads over the entire cross section of the oscillating tunnel, to reach the boundary layer at the bed.

The turbulence generated in this fashion may be different from that generated by a spilling breaker, and the present experimental investigation can therefore be considered to be an investigation of the more general problem of externally generated turbulence, rather than looking specifically at the turbulence generated by wave breaking or flow past structures. Nevertheless, the present investigation can shed light into the processes, which take place in the WBL when external turbulence is present. Rough bed boundaries are not considered in this investigation, and a purely oscillating flow is adopted to avoid complications caused by real waves, such as wave nonlinearity, wave asymmetry and the nonuniform external-turbulence generation, etc.

Numerous studies on smooth-wall, boundary layer flows were carried out in the past. The reader is referred to Jensen et al. (1989) for a review of the works on this subject. Jensen et al. (1989) complemented the previous works in that they conducted their experiments at a higher range of Reynolds numbers:

$$Re = \frac{U_{om}a}{\nu} \quad (1.1)$$

where U_{om} is the maximum value of the outer-flow velocity, a is the amplitude of the motion in the outer-flow and ν is the kinematic viscosity.

2. Experimental set-up

The measurements were carried out in a U-shaped oscillating-water tunnel. This tunnel is the same as that described by Jensen et al. (1989). The working section was 0.29 m in height and 0.39 m in width. The walls of the working section were made of smooth transparent perspex plates. The bottom of the flume, made of PVC plates, acted as a hydraulically smooth surface.

Fig. 2a shows a schematic description of the experimental set-up while a detailed sketch of the test section is shown in Fig. 2b. The difference between the present set-up and that used by Jensen et al. (1989) is that a series of grids, of dimensions 0.15 m in height and 0.39 m in width, were placed 5.5 cm apart and mounted to the top of the tunnel to generate external turbulence. The total length of the grid section was 6 m, located at the central part of the oscillating water tunnel, with 1.0 m contractions at the ends (Fig. 2b).

The grids were made of 1-mm-thick perforated plates. Two different grid porosities were used, with perforations made up of 0.5×0.5 cm and 4×4 cm square holes, for the low-porosity (Fig. 2c) and the high-porosity (Fig. 2d) grids, respectively.

The oscillatory flow in the tunnel was driven by an electronically controlled pneumatic system. In the tests, the period of oscillation was held constant at 9.72 s. This period is the same as that in the earlier WBL study, and corresponds to the tunnel's natural frequency. Although the natural frequency of the tunnel in the present study increased by up to 10% due to the presence of the grids (10.02 and 10.60 s in the case of the high-porosity and low-porosity grids, respectively), the frequency of 9.72 s was adopted to make comparisons on the same basis.

Two kinds of measurements were carried out: velocity and bed shear stress measurements. The velocities were measured by Laser-Doppler Anemometer (LDA). Two LDA systems were used in the study: a two-component system and a one-component system. The former consisted of 400 mW Argon laser in forward scatter mode with two Dantec 55N12 frequen-

Table 1
Test conditions

Test	Period (s)	U_{om} (m/s)	a (m)	ν (cm ² /s ²)	$Re = aU_{om}/\nu$	$Re_\delta = \delta U_{om}/\nu$	U_{fm} (cm/s)	Quantity measured	Apparatus	N	Δt (s)
1	9.72	0.085	0.133	0.0101	1.1×10^4	148	0.84	$\bar{\tau}_o, \sqrt{\tau_o'^2}, U_o$	Hot film, 1D-LDA	50	0.027
2	9.72	0.121	0.188	0.0101	2.2×10^4	210	1.06	$\bar{\tau}_o, \sqrt{\tau_o'^2}, U_o$	Hot film, 1D-LDA	50	0.027
3	9.72	0.160	0.245	0.0101	3.9×10^4	280	1.24	$\bar{\tau}_o, \sqrt{\tau_o'^2}, U_o$	Hot film, 1D-LDA	50	0.027
4	9.72	0.223	0.344	0.0101	7.6×10^4	390	1.48	$\bar{\tau}_o, \sqrt{\tau_o'^2}, U_o$	Hot film, 1D-LDA	50	0.027
5	9.72	0.287	0.460	0.0101	1.3×10^5	510	1.80	$\bar{\tau}_o, \sqrt{\tau_o'^2}, U_o$	Hot film, 1D-LDA	50	0.027
6	9.72	0.345	0.534	0.0101	1.8×10^5	600	2.18	$\bar{\tau}_o, \sqrt{\tau_o'^2}, U_o$	Hot film, 1D-LDA	50	0.027
7	9.72	0.380	0.610	0.0101	2.3×10^5	678	2.56	$\bar{\tau}_o, \sqrt{\tau_o'^2}, U_o$	Hot film, 1D-LDA	50	0.027
8	9.72	0.442	0.702	0.0101	3.1×10^5	787	2.88	$\bar{\tau}_o, \sqrt{\tau_o'^2}, U_o$	Hot film, 1D-LDA	50	0.027
9	9.72	0.637	1.030	0.0101	6.5×10^5	1140	4.17	$\bar{\tau}_o, \sqrt{\tau_o'^2}, U_o$	Hot film, 1D-LDA	50	0.027
10	9.72	1.040	1.669	0.0101	1.7×10^6	1840	6.35	$\bar{\tau}_o, \sqrt{\tau_o'^2}, U_o$	Hot film, 1D-LDA	50	0.027
11	9.72	1.065	1.650	0.0101	1.7×10^6	1840	–	$\bar{u}, \sqrt{u'^2}, \sqrt{v'^2}, \overline{u'v'}, U_o$	2D-LDA	50	0.027
12	9.72	1.065	1.650	0.0101	1.7×10^6	1840	–	$\bar{u}, \sqrt{u'^2}, \sqrt{v'^2}, \overline{u'v'}, U_o$	2D-LDA	5	0.0012

Low-porosity grid.

Table 2
Test conditions

Test	Period (s)	U_{om} (m/s)	a (m)	ν (cm ² /s ²)	$Re = aU_{om}/\nu$	$Re_\delta = \delta U_{om}/\nu$	U_{fm} (cm/s)	Quantity measured	Apparatus	N	Δt (s)
1	9.72	0.088	0.137	0.0105	1.2×10^4	155	0.86	$\bar{\tau}_o, \sqrt{\tau_o'^2}, U_o$	Hot film, 1D-LDA	50	0.027
2	9.72	0.107	0.165	0.0105	1.7×10^4	184	0.97	$\bar{\tau}_o, \sqrt{\tau_o'^2}, U_o$	Hot film, 1D-LDA	50	0.027
3	9.72	0.139	0.215	0.0105	2.9×10^4	241	1.08	$\bar{\tau}_o, \sqrt{\tau_o'^2}, U_o$	Hot film, 1D-LDA	50	0.027
4	9.72	0.209	0.324	0.0105	6.5×10^4	360	1.33	$\bar{\tau}_o, \sqrt{\tau_o'^2}, U_o$	Hot film, 1D-LDA	50	0.027
5	9.72	0.291	0.450	0.0105	1.3×10^5	510	1.57	$\bar{\tau}_o, \sqrt{\tau_o'^2}, U_o$	Hot film, 1D-LDA	50	0.027
6	9.72	0.399	0.617	0.0105	2.3×10^5	678	2.10	$\bar{\tau}_o, \sqrt{\tau_o'^2}, U_o$	Hot film, 1D-LDA	50	0.027
7	9.72	0.467	0.722	0.0105	3.2×10^5	800	2.56	$\bar{\tau}_o, \sqrt{\tau_o'^2}, U_o$	Hot film, 1D-LDA	50	0.027
8	9.72	0.553	0.855	0.0105	4.5×10^5	950	3.19	$\bar{\tau}_o, \sqrt{\tau_o'^2}, U_o$	Hot film, 1D-LDA	50	0.027
9	9.72	0.651	1.007	0.0105	6.2×10^5	1110	3.91	$\bar{\tau}_o, \sqrt{\tau_o'^2}, U_o$	Hot film, 1D-LDA	50	0.027
10	9.72	0.763	1.180	0.0103	8.7×10^5	1320	4.33	$\bar{\tau}_o, \sqrt{\tau_o'^2}, U_o$	Hot film, 1D-LDA	50	0.027
11	9.72	1.087	1.681	0.0103	1.79×10^6	1890	6.26	$\bar{\tau}_o, \sqrt{\tau_o'^2}, \bar{u}, \sqrt{u'^2}, \sqrt{v'^2}, \overline{u'v'}, U_o$	Hot film, 2D-LDA	50	0.027
12	9.72	1.342	2.076	0.0105	3.0×10^6	2450	7.47	$\bar{\tau}_o, \sqrt{\tau_o'^2}, U_o$	Hot film, 1D-LDA	50	0.027
13	9.72	1.659	2.567	0.0105	4.4×10^6	2970	8.48	$\bar{\tau}_o, \sqrt{\tau_o'^2}, U_o$	Hot film, 1D-LDA	50	0.027
14	9.72	1.087	1.681	0.0103	1.79×10^6	1890	–	$\bar{u}, \sqrt{u'^2}, \sqrt{v'^2}$	Hot film, 2D-LDA	5	0.0012

High-porosity grid.

cy shifters and two Dantec 55N21 frequency trackers. To minimize the mismatch of the two pairs of laser beams in the two-component velocity measurements, the laser beams were set at an angle of 45° to the flow direction. The one-component laser system was mainly used to measure the reference horizontal velocity signal. The one-component system consisted of a 15 mW Argon laser in forward scatter mode, using a similar frequency shifter and a frequency tracker.

The bed shear stress was measured, using a Dantec 55R-46 hot film probe (similar to Jensen et al., 1989). The probe was flush-mounted to the bed close to the centre line of the tunnel, as shown in Fig. 2b. The working principle of the hot film technique is that if the hot-film element is fed with a current source, the voltage required to maintain a constant temperature is related to the gradient of the instantaneous velocity at the wall and hence the wall shear stress. This relation is expressed as $\tau_o^{1/3} = AE^2 + B$ in which τ_o is the wall shear stress, A and B are constants which have to be found by calibrating the probe, and E is the voltage. The calibration of the hot-film probe was carried out in-position, using a three-sided channel (1.5 mm in depth and 30 mm width), which was placed over the probe and water pumped through the channel. Details regarding the hot-film probe, the calibration, and other pertinent information can be found in Sumer et al. (1993).

The movement of the free surface in the open riser was monitored with a wave gauge. This signal was used as a reference signal in data processing.

In a majority of cases, the sampling interval, Δt , was 27 ms (corresponding to 1° sampling interval in phase). The total number of cycles, N , sampled was 50. This was changed in Test 12 (Table 1) and Test 14 (Table 2) for both experiments with the grids and Test 2 (Table 3) for a supplementary test carried out for the undisturbed case. In these cases, a sampling interval

of 1.2 ms was used, and the number of cycles sampled was $N=5$. The specific goal of these tests was to obtain information on the correlation of turbulence.

Mean and r.m.s. values of the measured quantities were calculated through ensemble averaging.

3. Test conditions

Tables 1 and 2 present the test conditions for the low-porosity and high-porosity grids, respectively. Table 3 presents the test conditions for the undisturbed case. u and v are the velocity components in the x - and y -directions, respectively (Fig. 1). U_{om} is the amplitude of the velocity at the outer edge of the bed boundary layer defined by:

$$U_o = U_{om} \sin(\omega t) \quad (3.1)$$

in which ω is the angular frequency, $\omega = 2\pi/T$ (T being the period of the oscillatory motion). Furthermore, a is the amplitude of motion corresponding to $a = U_{om}T/(2\pi)$, τ_o is the bed shear stress, u' , v' and τ_o' , respectively, are the fluctuating values of u , v and τ_o while quantities with an overbar are ensemble averaged quantities, defined by:

$$\bar{\phi}(\omega t) = \frac{1}{N} \sum_{i=1}^N \phi\{\omega[t + (i-1)T]\} \quad (3.2)$$

$$\overline{\phi'^2}(\omega t) = \frac{1}{N-1} \sum_{i=1}^N \{\phi\{\omega[t + (i-1)T]\} - \bar{\phi}\{\omega[t + (i-1)T]\}\}^2 \quad (3.3)$$

where the symbol, ϕ , is used to denote a measured quantity.

Table 3
Test conditions—undisturbed case

Test	Period (s)	U_{om} (m/s)	a (m)	v (cm^2/s^2)	$Re = aU_{om}/\nu$	$Re_\delta = \delta U_{om}/\nu$	U_{fm} (cm/s)	Quantity measured	Apparatus	N	Δt (s)
1	9.72	1.097	1.697	0.0108	1.72×10^6	1855	5.13	$\bar{\tau}_o, \sqrt{\overline{\tau_o'^2}}, \bar{u}, \sqrt{\overline{u'^2}}, \sqrt{\overline{v'^2}}, \overline{u'v'}, U_o$	Hot film, 2D-LDA	50	0.027
2	9.72	1.097	1.697	0.0108	1.72×10^6	1855	–	$\bar{u}, \sqrt{\overline{u'^2}}, \sqrt{\overline{v'^2}}$	Hot film, 2D-LDA	5	0.0012

Re_δ is the Reynolds number based on the laminar boundary layer thickness,

$$Re_\delta = \frac{U_{om}\delta}{\nu}$$

in which δ , the laminar boundary layer thickness,

$$\delta = \sqrt{\frac{2\nu}{\omega}}$$

Note that the relationship between Re (Eq. (1.1)) and Re_δ is $Re_\delta = \sqrt{2Re}$.

U_{fm} is the maximum value of the bed shear velocity given by:

$$U_{fm} = \sqrt{\frac{\bar{\tau}_{om}}{\rho}} \tag{3.4}$$

in which $\bar{\tau}_{om}$ is the maximum value of the bed shear stress defined by:

$$\bar{\tau}_o = \bar{\tau}_{om}f(\omega t + \varphi) \tag{3.5}$$

In Eq. (3.5), φ is the phase lead of the zero up-crossing of the bed shear stress over the velocity U_o .

4. Bed shear stress

4.1. Transition to turbulence

Fig. 3 presents the time series of the bed shear stress for four different Re numbers together with those of the reference velocity U_o (Fig. 1). For brevity, only the result for the experiments with the low-porosity grid is presented. Transition-to-turbulence occurs in the form of spikes in the bed shear stress signal (marked with arrows in Fig. 3b,c) just prior to flow reversals, in exactly the same fashion as that described in Hino et al. (1976) and Jensen et al. (1989) (the undisturbed case). The way in which the transition occurs in the case of the high-porosity grid is the same as in Fig. 3.

The present experiments show that the transition-to-turbulence in the bed shear stress first takes place when the Reynolds number reaches a value of 7×10^4 . For the high-porosity grid, the corresponding Reynolds number for transition-to-turbulence was found to be 1.3×10^5 . The critical Reynolds number

for transition-to-turbulence in the undisturbed case is around 1.6×10^5 (Jensen et al., 1989). As can be seen, the present value obtained with the low-porosity grid, 7×10^4 , is a factor of 2.3 smaller than the critical value found in the undisturbed case while that obtained with the high-porosity grid, 1.3×10^5 , is only 1.2 times smaller. This illustrates the influence of the outer flow turbulence on the transition-to-turbulence in the bed boundary layer, in agreement with the results obtained from steady boundary layer flow research (Schlichting, 1979, p. 451).

4.2. Mean and fluctuating bed shear stress

Figs. 4 and 5 present the phase variation of the mean bed shear stress, $\bar{\tau}_o$, and r.m.s. value of the fluctuating bed shear stress, $\sqrt{\tau_o'^2}$, for the low-porosity grid experiments for different Re numbers. Also included in Fig. 5h are the corresponding results of $\sqrt{\tau_o'^2}$ for the high-porosity grid and undisturbed cases. $\sqrt{\tau_o'^2}$ is not normalized by $\bar{\tau}_{om}$ in Fig. 5, to emphasize the increase in the r.m.s. value as the Reynolds number is increased.

The features observed in Figs. 4 and 5 are quite similar to those of the undisturbed case reported in Jensen et al. (1989), namely (i) the phase lead of the bed shear stress decreases with increasing Re (Fig. 4), and (ii) turbulence spreads towards the smaller phases with increasing Re (Fig. 5).

Fig. 6 presents the maximum value of $\left(\sqrt{\tau_o'^2}\right)$ normalized by $\bar{\tau}_{om}$ as a function of Re , both in the present case with grids and in the case of without grids (Jensen et al., 1989). The result obtained for the supplementary test, for the undisturbed case, at $Re = 1.72 \times 10^6$ is also shown. The figure reveals that: (i) the transition to turbulence occurs earlier in the present grid cases; and (ii) the relative intensity of turbulence in the bed shear stress increases with the presence of the grids. It is seen that the externally generated turbulence is able to penetrate the bed boundary layer, and this penetration of turbulence near the bed would result in changes to the resistance characteristics of the flow, as will be seen in the following subsection. (It may be noted that the maxima experienced at $Re = 2.3 \times 10^5$ are due to the presence of turbulent spikes in the transition regime; see arrows in Fig. 3c.)

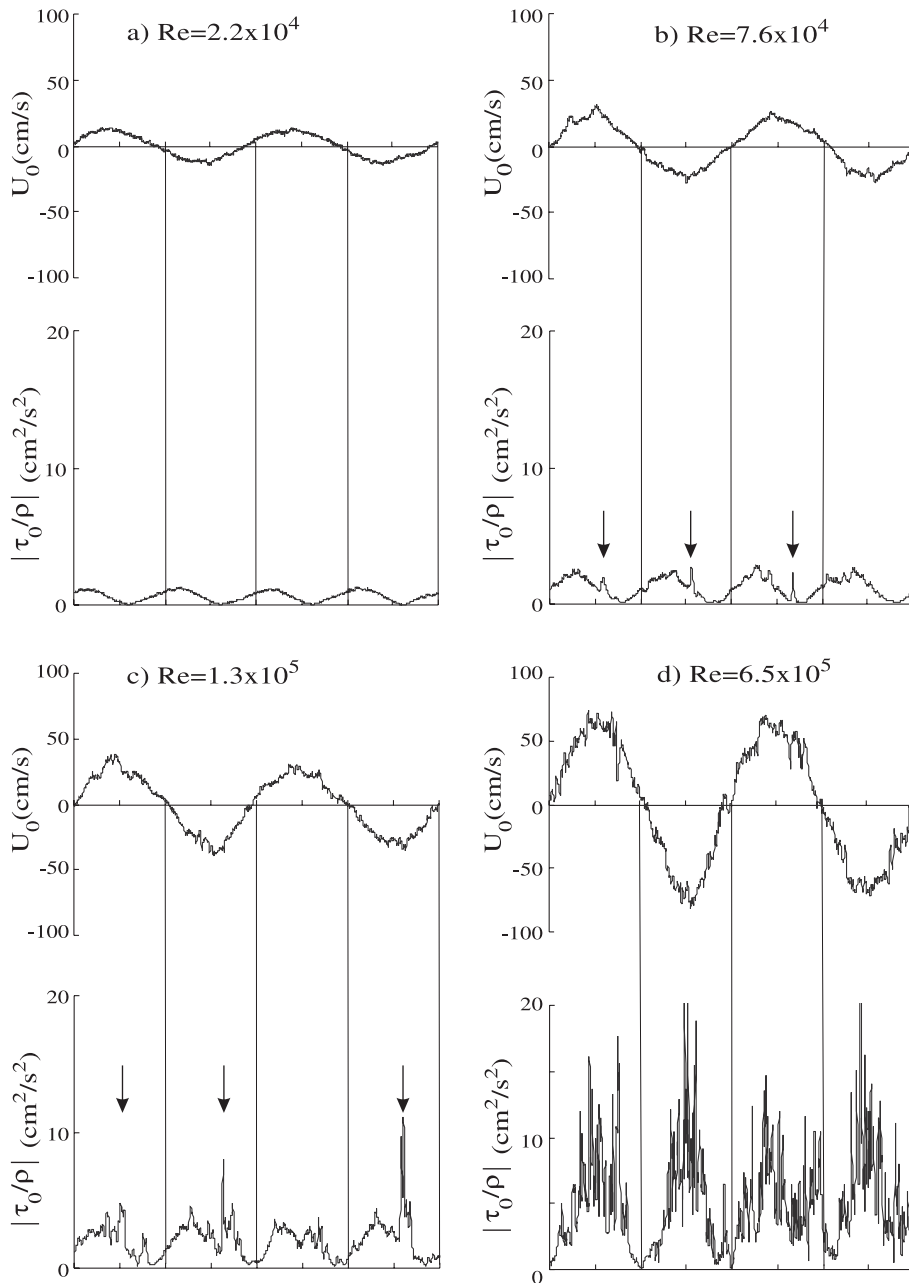


Fig. 3. Time series of the reference velocity, U_0 , and the bed shear stress, $|\tau_0/\rho|$. Low-porosity grid, Tests 2, 4, 5 and 9.

To be able to observe the way in which the externally generated turbulence penetrates the boundary layer, a flow visualization study was conducted. Dye was released through a nozzle

located at the tip of the grids (Fig. 7), and the flow made visible by the dye was videotaped during one-half cycle of the motion. The grid was the high-porosity grid in the test. Fig. 8 displays a sequence

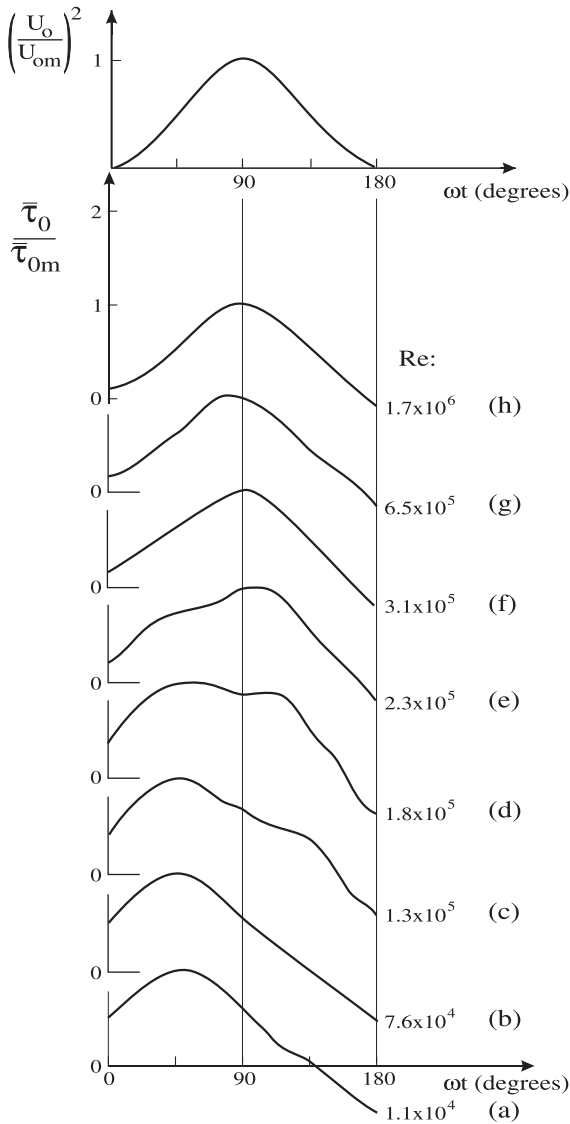


Fig. 4. Phase variation of the mean bed shear stress over one-half cycle of the motion for various Re . Low-porosity grid, Tests 1, 4–10.

of video frames illustrating the flow from $\omega t = 84^\circ$ to 140° . For comparison, a video frame (corresponding to $\omega t = 100^\circ$) obtained in the case of the undisturbed flow is also given (Fig. 9). The flow conditions in this latter test were exactly the same as in Fig. 8.

It is seen from Fig. 8 that coherent vortices (R, S, ...) emanating from the grid region penetrate the

boundary layer. It is clear from the figure that these vortices can reach the bottom, and therefore influence the bed shear stress. Fig. 10a reveals this. Successive crests and troughs (Crests A', B', C', ..., H' and Troughs J', K', L', ..., P') in the bed-shear-stress signal are the "signatures" of the vortices reaching the bed. Notice the same features in the velocity signal, namely the "signatures" of the latter vortices. (Note that the measurement point was located at $y = 29$ mm.) Clearly the bed shear stress associated with the bound-

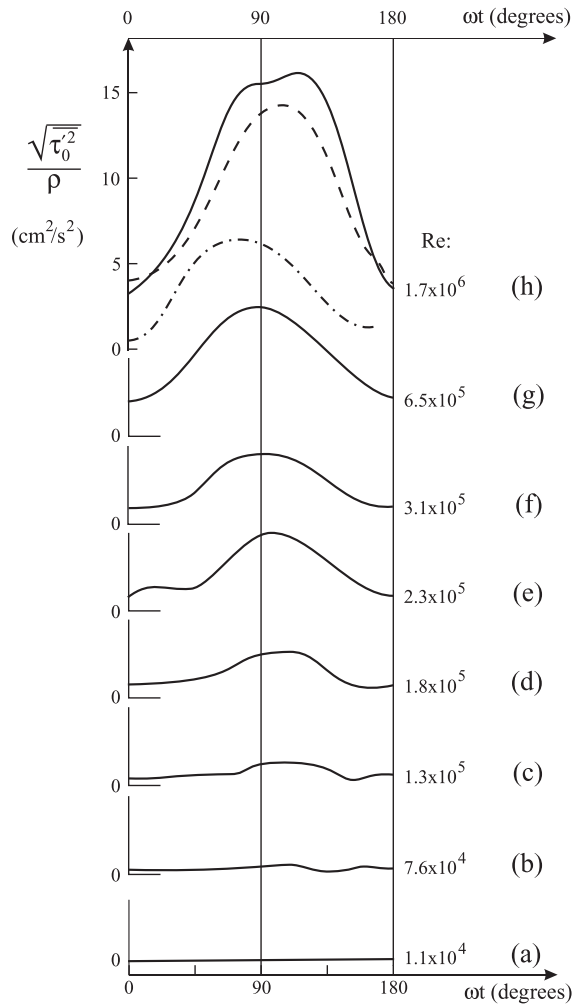


Fig. 5. Phase variation of the r.m.s. value of the bed shear stress fluctuations over one-half cycle of the motion for various Re . Low-porosity grid, Tests 1, 4–10. Also included in (h) are the corresponding results for the high-porosity grid case (dashed line) and undisturbed case (dashed-dotted line).

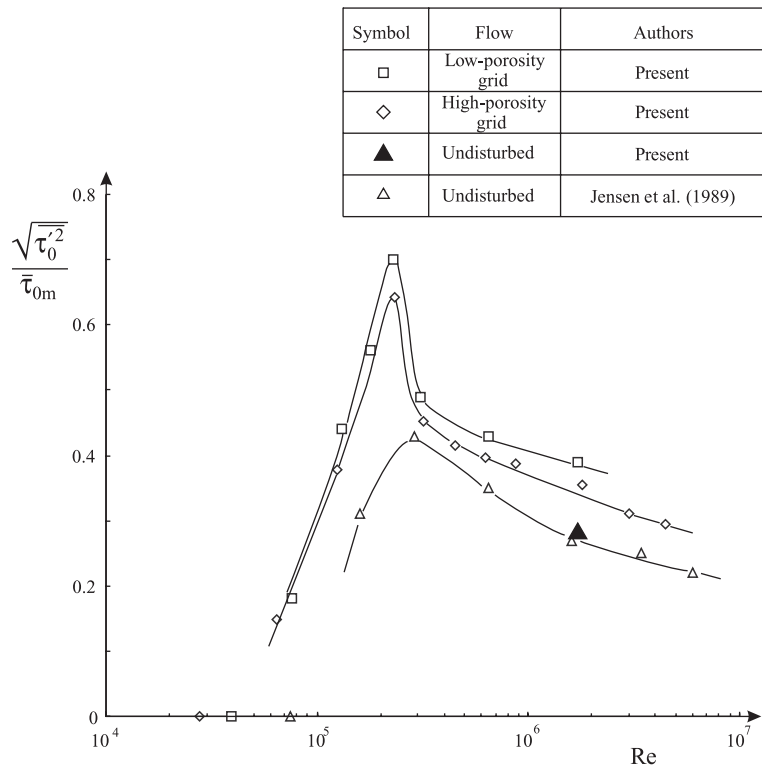


Fig. 6. Normalized maximum r.m.s. values of the bed shear stress fluctuations as a function of Re .

ary layer flow (Fig. 10b) is heavily influenced by the vortices generated by the grids (Fig. 10a). It may be noted that the mean period of the quasi-cyclic signals

in Fig. 10a, namely 0.44 s, is in accord with that of the passage of the vortices at the measurement section in Fig. 8, namely about 0.4 s.

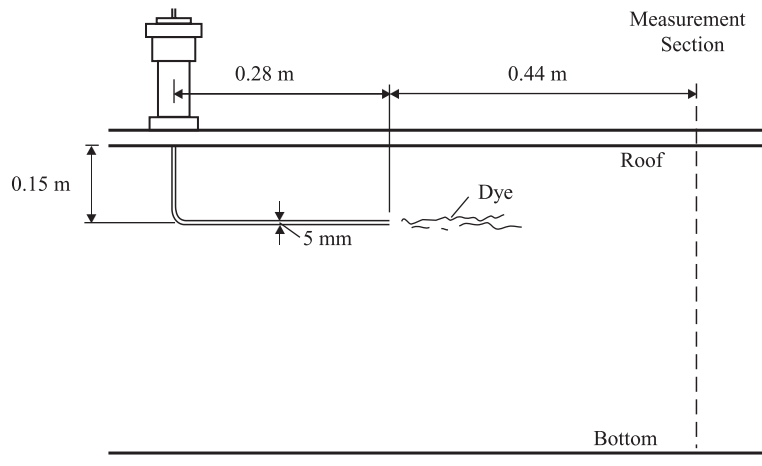


Fig. 7. Sketch illustrating the arrangement for the flow visualization study.

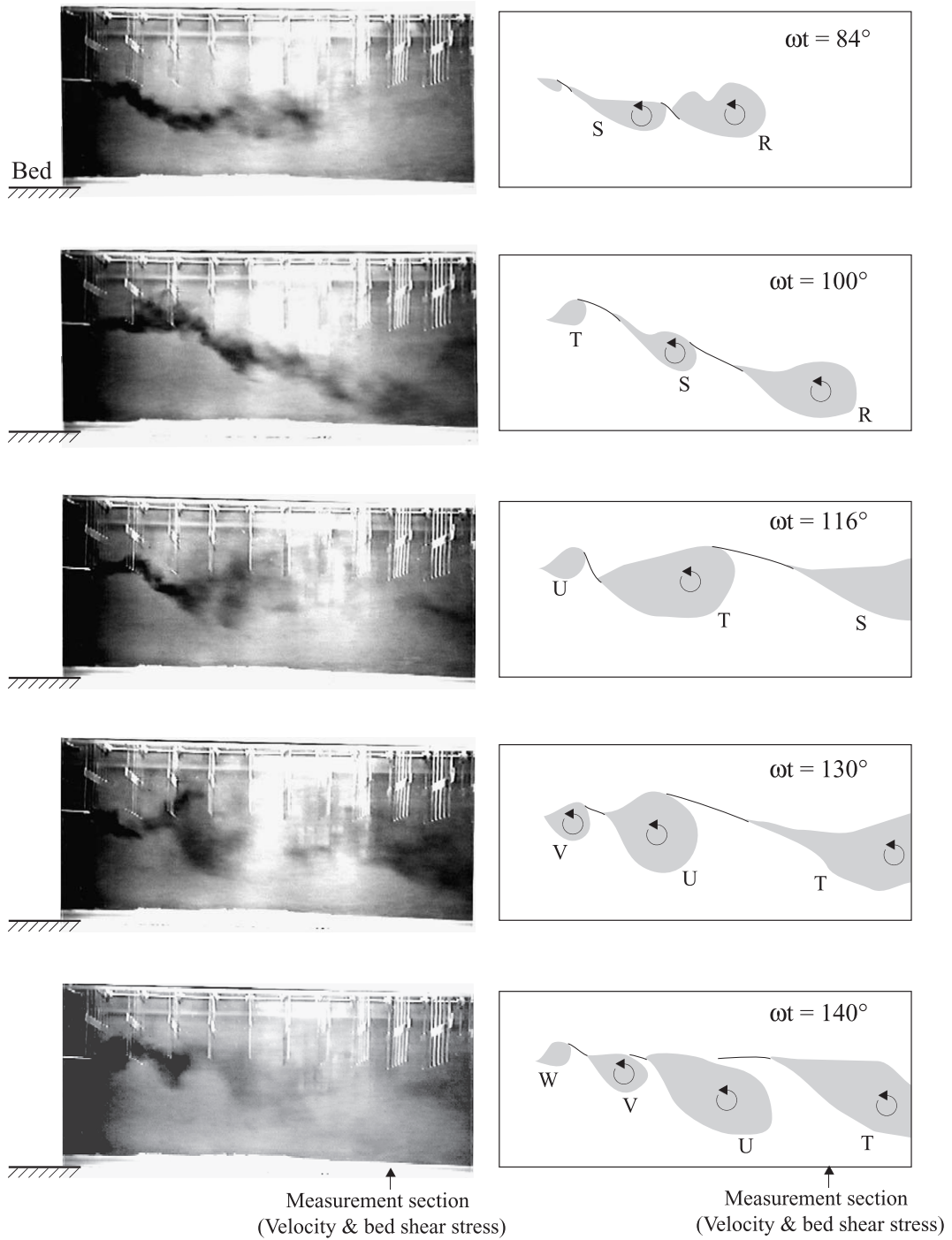


Fig. 8. A sequence of video frames illustrating the way in which turbulence is generated. Vortices R, S, ... are shed from the tips of the grids. High-porosity grid. $Re = 1.72 \times 10^6$.

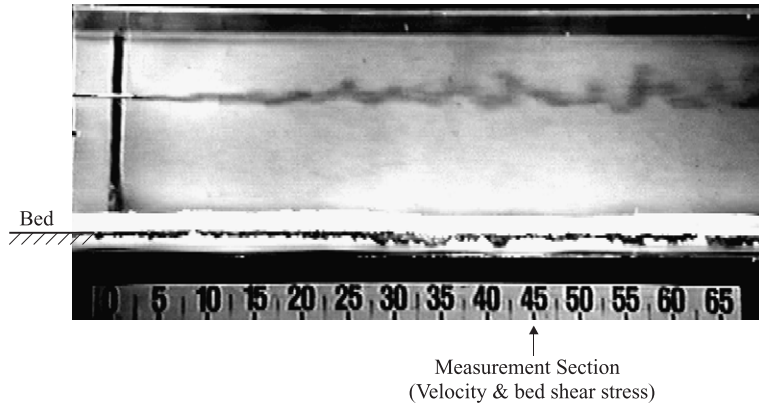


Fig. 9. A video frame illustrating the flow/turbulence in the case of the undisturbed flow. $Re=1.72 \times 10^6$.

4.3. Friction coefficient and phase lead

The friction coefficient:

$$f_w = 2 \frac{\bar{\tau}_{om}/\rho}{U_{om}^2} \quad (4.1)$$

obtained in the present study with grids is compared with that corresponding to the ordinary oscillatory boundary layer (Jensen et al., 1989) in Fig. 11. The result obtained for the present undisturbed test, at $Re=1.72 \times 10^6$, is also shown. The solid line represents the laminar solution $f_w = 2/\sqrt{Re}$. The friction factor in the present grid experiments, when the flow ceases to be laminar, undergoes a substantial increase over the results of turbulent WBL (Jensen et al., 1989). This is linked to the increased momentum exchange caused by the external turbulence, which is able to penetrate the bed boundary layer, as demonstrated in the previous section. In the case of laminar regime boundary layer flow, however, no change in f_w occurs, due to the absence of an external turbulence field revealed by the LDA measurements as will be discussed later.

Fig. 12 presents data related to the phase lead, φ , of the bed shear stress over the velocity at the outer edge of the bed boundary layer (see the definition sketch in Fig. 11). The data from Jensen et al. (1989) corresponding to the case of the normal oscillatory boundary layer, together with the theoretical solutions for the laminar boundary layer and the fully developed turbulent layer (Fredsøe, 1984), are also included for

comparison. The φ -versus- Re curve for the experiments using the grids is shifted towards the left of Jensen et al.'s (1989) data. This is again linked to the

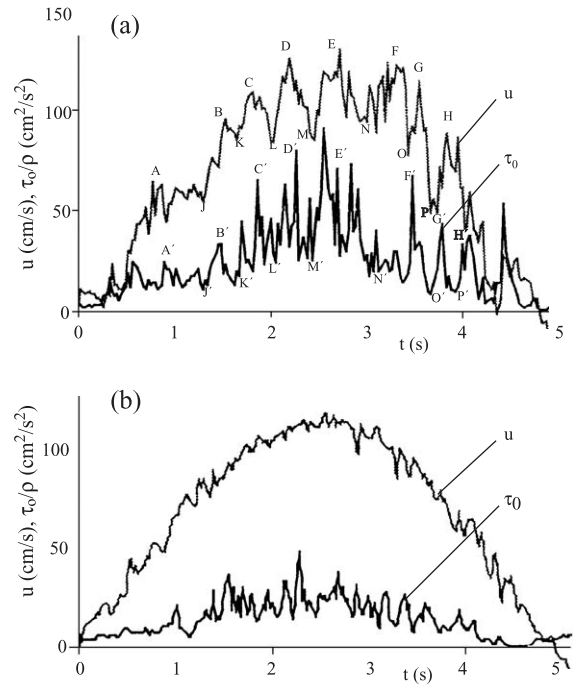


Fig. 10. Time series of the velocity at the outer edge of the boundary layer and that of the bed shear stress over one-half cycle of the motion. Flow conditions are exactly the same as in Figs. 8 and 9. (a) High-porosity grid (cf. Fig. 8). (b) Undisturbed case (cf. Fig. 9). $Re=1.72 \times 10^6$.

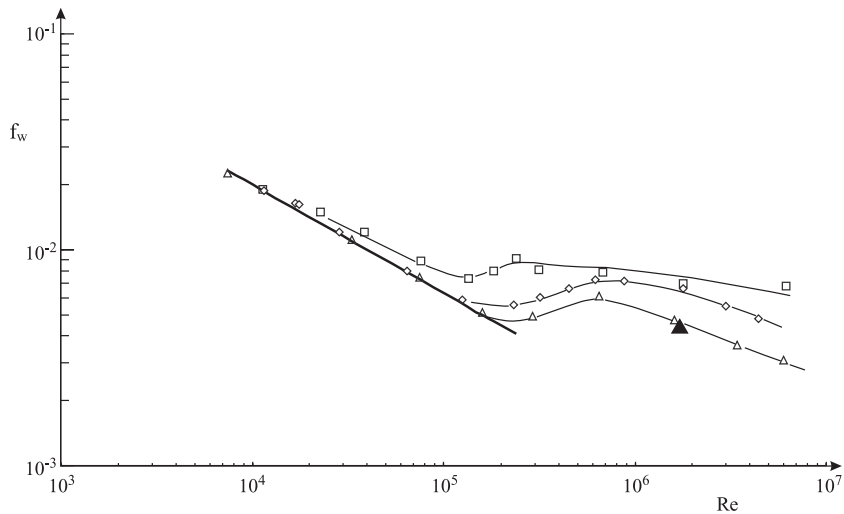


Fig. 11. Friction coefficient versus Re . The solid line represents the laminar solution $f_w = 2/\sqrt{Re}$. See Fig. 6 for the symbols.

early transition to turbulence. The data in the figure further show that the phase lead becomes rather small, $O(5^\circ)$, at large Reynolds numbers. This is caused by

the enhanced momentum exchange between the bed and the outer flow. The larger the momentum exchange, the smaller the phase difference.

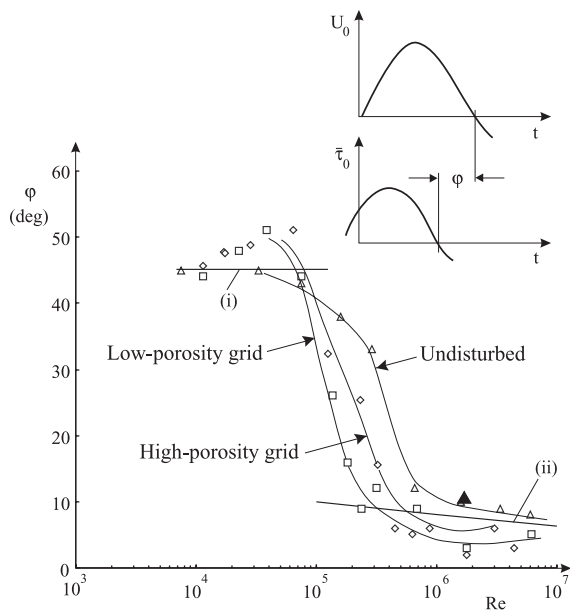


Fig. 12. Phase lead of the bed shear stress over the outer-flow velocity. (i) The laminar flow solution is indicated by a horizontal line at $\phi = 45^\circ$. (ii) Solution for the fully developed turbulent boundary layer (Fredsøe, 1984). See Fig. 6 for the symbols.

5. Mean and fluctuating velocity profiles

5.1. Outer-flow representation

Fig. 13 presents the mean velocity distribution for the present grid measurements (Test 11, Table 1 and Test 11, Table 2). As a comparison, the velocity distribution for the undisturbed case (Test 1, Table 3) is also included. Figs. 14–16 display the turbulence quantities, $\overline{u'v'}$, $\sqrt{u'^2}$ and $\sqrt{v'^2}$, respectively. The following observations can be made:

1. The velocity distribution is significantly altered due to the presence of the grids. It can be seen that in addition to the bed boundary layer, a shear layer exists near the grids;
2. The velocity distributions for the two grid cases are similar; and
3. $\overline{u'v'}$, $\sqrt{u'^2}$ and $\sqrt{v'^2}$ are increased significantly over the undisturbed case.

It may be noted that though the $\overline{u'v'}$, $\sqrt{u'^2}$ and $\sqrt{v'^2}$ values for the grid experiments are similar for

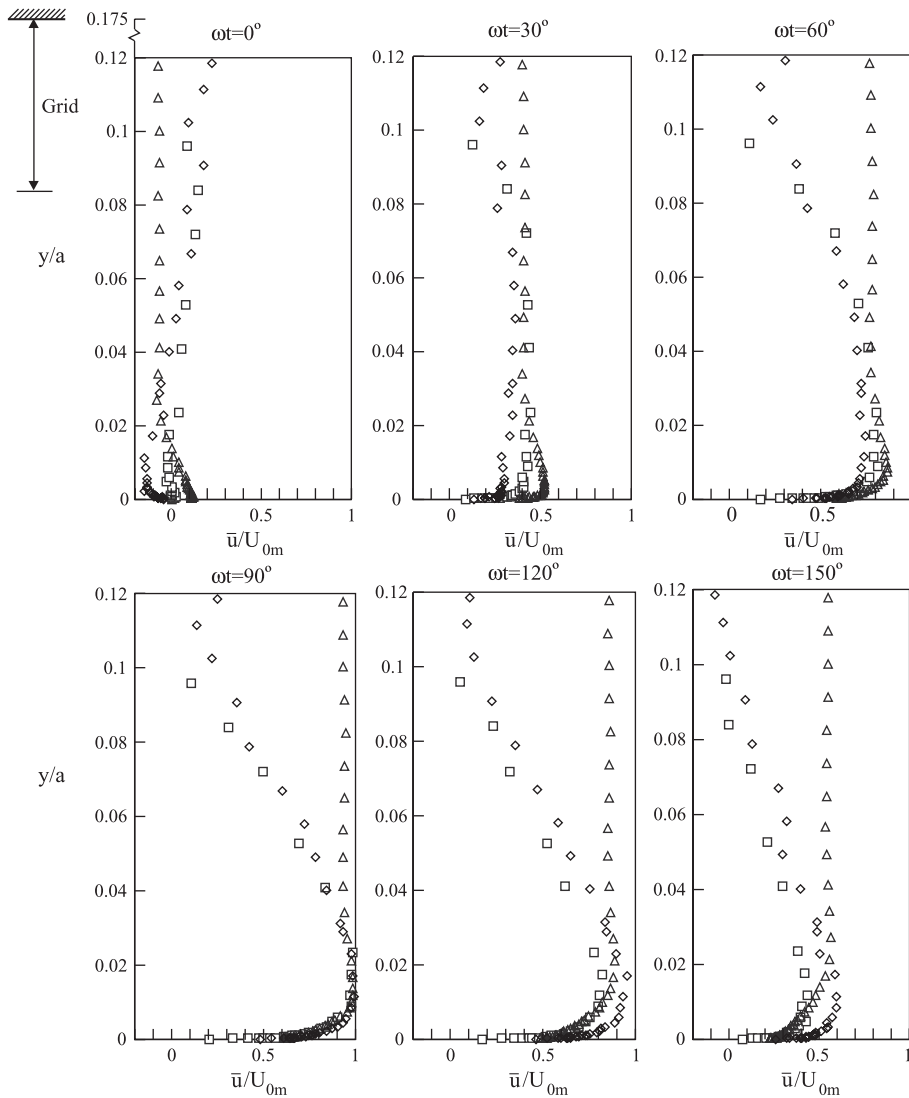


Fig. 13. Mean velocity distributions. Squares: low-porosity grid, Test 11, Table 1, $Re = 1.74 \times 10^6$; diamonds: high-porosity grid, Test 11, Table 2, $Re = 1.79 \times 10^6$; triangles: undisturbed case, Test 1, Table 3, $Re = 1.72 \times 10^6$.

the two cases, the high-porosity grid values, from $\omega t \approx 150^\circ$ to 60° , appear to be slightly larger than the low-porosity grid values. No clear explanation has been found for this behavior.

Figs. 17 and 18 present the near-bed close-up pictures of the mean velocity and the Reynolds stress distributions, respectively (cf. Figs. 13 and 14).

5.1.1. Discussion on the shear stresses in the outer flow

The generation of turbulence due to the grid is, to a large extent, associated with the growth of a thick boundary layer adjacent to the grid at each half cycle. The development of this outer boundary layer can be seen in the time evolution of the mean velocity and the Reynolds stress depicted in Figs. 13 and 14. After

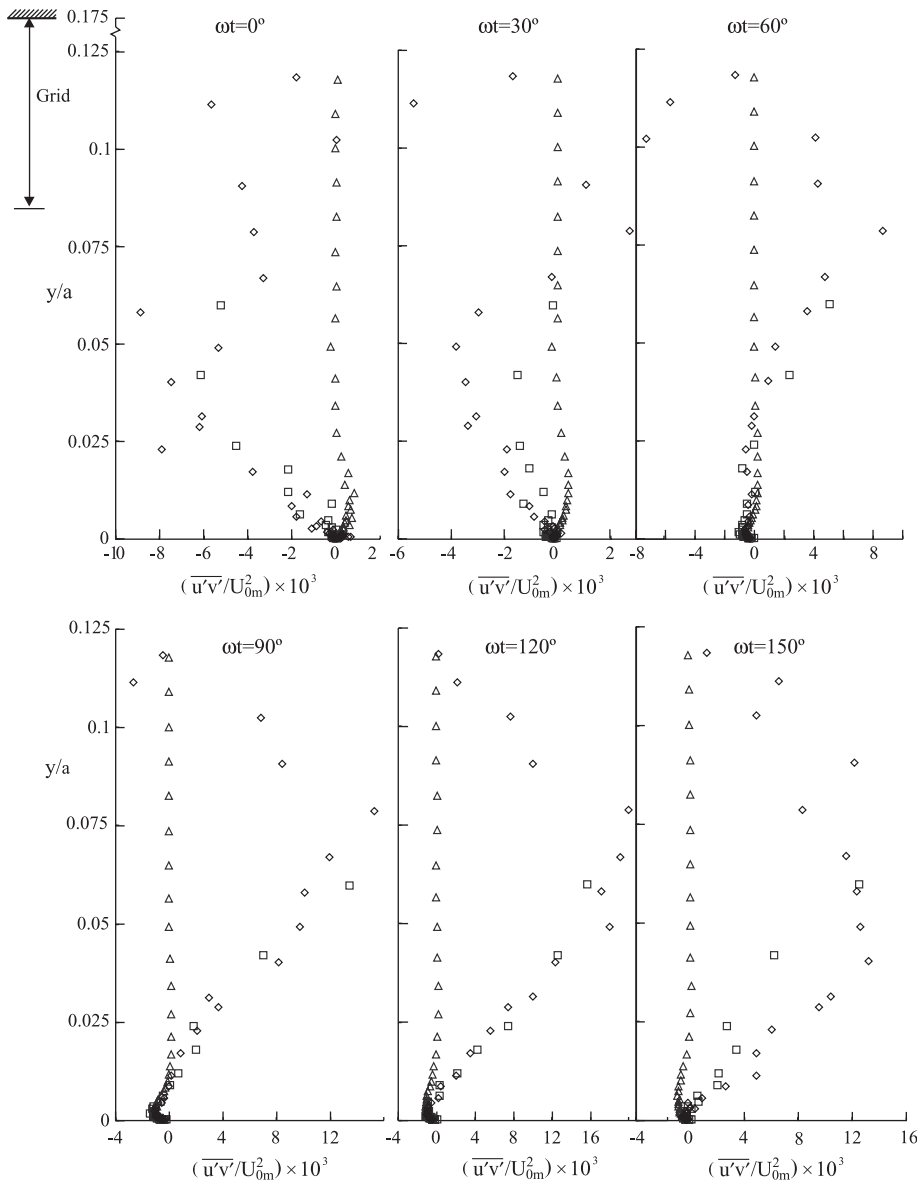


Fig. 14. Distributions of $\overline{u'v'}/U_{0m}^2$. Squares: low-porosity grid, Test 11, Table 1, $Re = 1.74 \times 10^6$; diamonds: high-porosity grid, Test 11, Table 2, $Re = 1.79 \times 10^6$; triangles: undisturbed case, Test 1, Table 3, $Re = 1.72 \times 10^6$.

the flow reversal, from $\omega t = 30^\circ$, the growth of the boundary layer from the lower edge of the grid can be seen (1) in the deficit in the mean velocity and (2) in the positive values of $\overline{u'v'}$.

As seen, there are significant shear stresses in the outer boundary layer. Therefore, the development in the shear stress and the velocity distribution in the

outer boundary layer has to be taken into account when considering the force balance of the flow.

Three elements in the horizontal force balance are considered:

$$\frac{\partial u}{\partial t} = -\frac{1}{\rho} \frac{\partial p}{\partial x} - \frac{\partial \overline{u'v'}}{\partial z}. \quad (5.1)$$

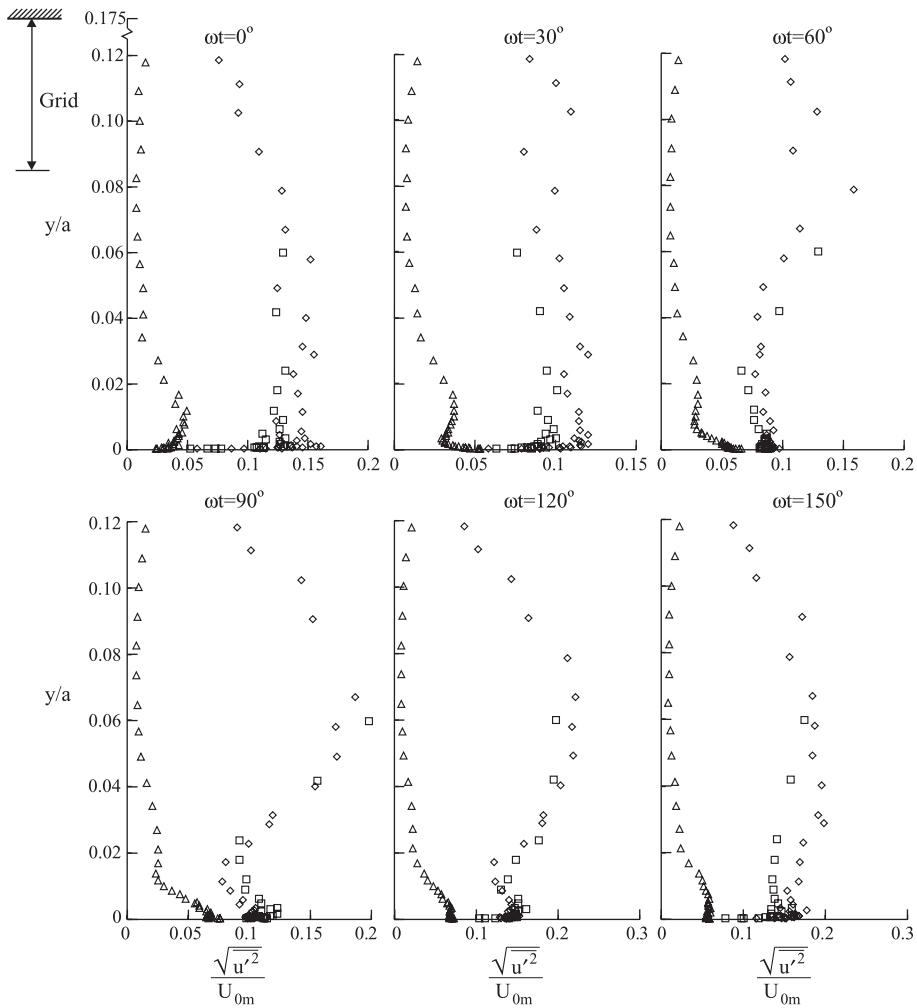


Fig. 15. Distributions of $\sqrt{u'^2}$. Squares: low-porosity grid, Test 11, Table 1, $Re = 1.74 \times 10^6$; diamonds: high-porosity grid, Test 11, Table 2, $Re = 1.79 \times 10^6$; triangles: undisturbed case, Test 1, Table 3, $Re = 1.72 \times 10^6$.

The force balance has been analyzed by integrating the above equation over a near-bed layer. The terms in the integrated force balance during one cycle of the motion are obtained from the measurements, and displayed in Fig. 19 for the two grid cases, namely for the low-porosity and high-porosity grids. The thickness of the near-bed layer in this exercise has been taken as $0.02a$. (The acceleration term has been calculated from the measured velocity profiles. The Reynolds stress term has been calculated from the measured Reynolds stress profiles. Given the acceleration and the Reynolds stress terms, the pressure-gradient term has been calculated from the integrated

force-balance equation.) To check the sensitivity to the thickness of the near-bed layer, the previously mentioned exercise has been repeated for another thickness of the near-bed layer, namely for $0.06a$. The results for this latter exercise have also been plotted in the same diagram (Fig. 19) (The empty triangle symbols in Fig. 19 indicating $-(1/\rho)(\partial p/\partial x)$ for the near-bed layer thickness of $0.02a$, and the filled triangle symbols the same quantity for the near-bed layer thickness of $0.06a$.) It should be noted that, except around $\omega t = 90^\circ$ and $\omega t = 270^\circ$, the bed shear stress is of minor importance for the total balance, and that the viscous stress at the top of the layer is negligible.

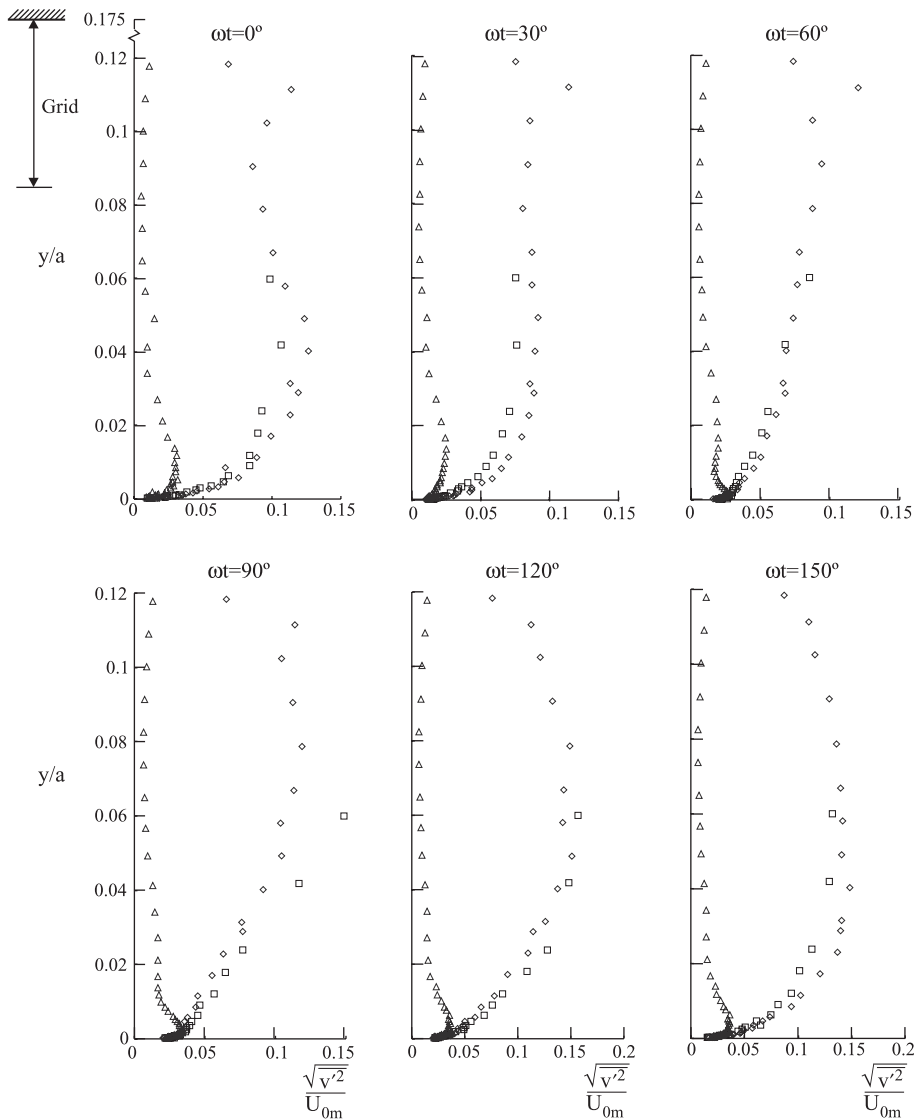


Fig. 16. Distributions of $\sqrt{v'^2}$. Squares: low-porosity grid, Test 11, Table 1, $Re = 1.74 \times 10^6$; diamonds: high-porosity grid, Test 11, Table 2, $Re = 1.79 \times 10^6$; triangles: undisturbed case, Test 1, Table 3, $Re = 1.72 \times 10^6$.

Now, as seen from Fig. 19, the Reynolds stresses give a maximum contribution corresponding to about 25% of the maximum flow acceleration. A significant lag is introduced between the acceleration and the pressure gradient, indicating that the energy is delivered to the system through the work of the pressure gradient to compensate for the energy dissipated through the Reynolds stresses.

The time variation of the Reynolds stress contribution to the force balance is related to the development of the outer boundary layer. It is changing sign during the first quarter cycle while the free stream velocity is accelerating and the near-bed boundary layer is being formed. This is in agreement with the observation that the outer boundary layer does not reach and interact with the bed boundary layer until

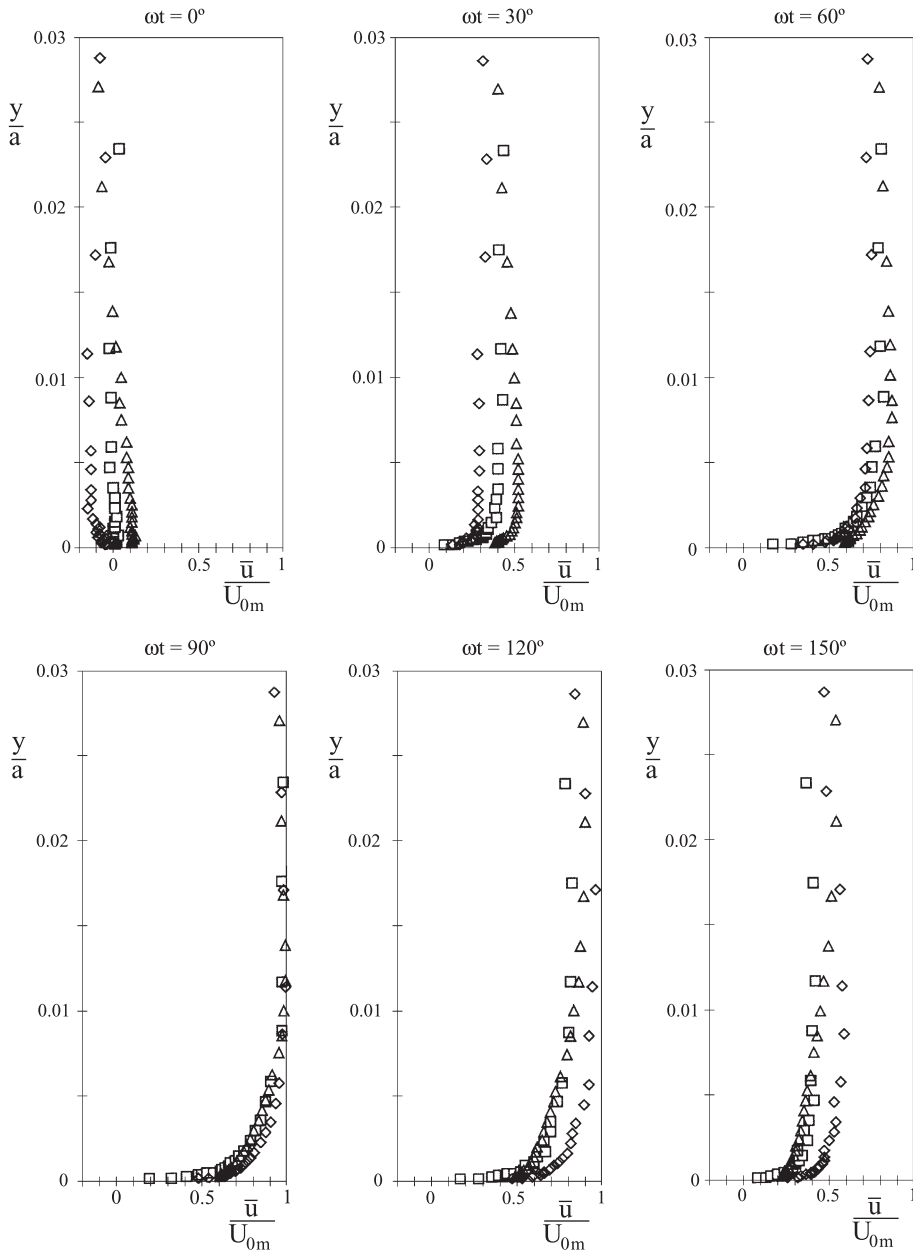


Fig. 17. Mean velocity distributions. Close-up. Squares: low-porosity grid, Test 11, Table 1, $Re=1.74 \times 10^6$; diamonds: high-porosity grid, Test 11, Table 2, $Re=1.79 \times 10^6$; triangles: undisturbed case, Test 1, Table 3, $Re=1.72 \times 10^6$.

after the free stream velocity has peaked. The impact of the Reynolds stress associated with the outer boundary layer on the bed boundary layer can be assessed from Fig. 18. Just after the flow reversal, the Reynolds shear stress outside the boundary layer is

positive as a remnant of the outer boundary layer in the previous half cycle. At $\omega t = 60^\circ$ and 90° the near-bed shear stresses are almost identical for the situations with and without an outer grid. At 120° , the shear stresses inside the bottom boundary layer begin

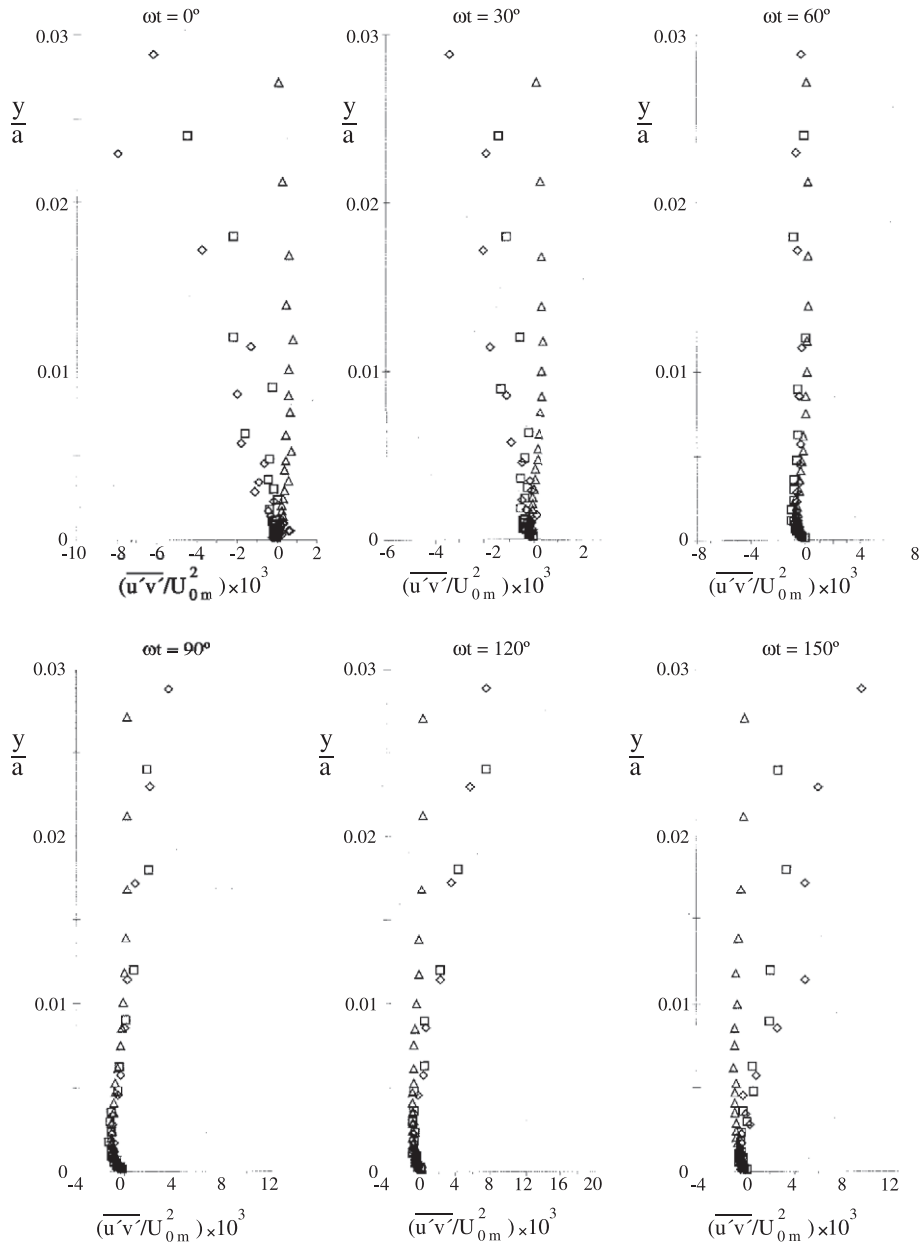


Fig. 18. Distributions of $\overline{u'v'}/U_{0m}^2$. Close-up. Squares: low-porosity grid, Test 11, Table 1, $Re=1.74 \times 10^6$; diamonds: high-porosity grid, Test 11, Table 2, $Re=1.79 \times 10^6$; triangles: undisturbed case, Test 1, Table 3, $Re=1.72 \times 10^6$.

to deviate from the shear stress without a grid, and the shear stress associated with the outer boundary layer does not reach the bed until at 150° phase angle.

The turbulence generated by the grid in the oscillating water tunnel will deviate from the con-

ditions in a surf zone. One difference is found in the shear stresses. In the present experiments, the two half cycles are symmetrical with reversal of the shear stress and a mean shear stress of zero. In a surf zone, the outer turbulence is mainly generated in

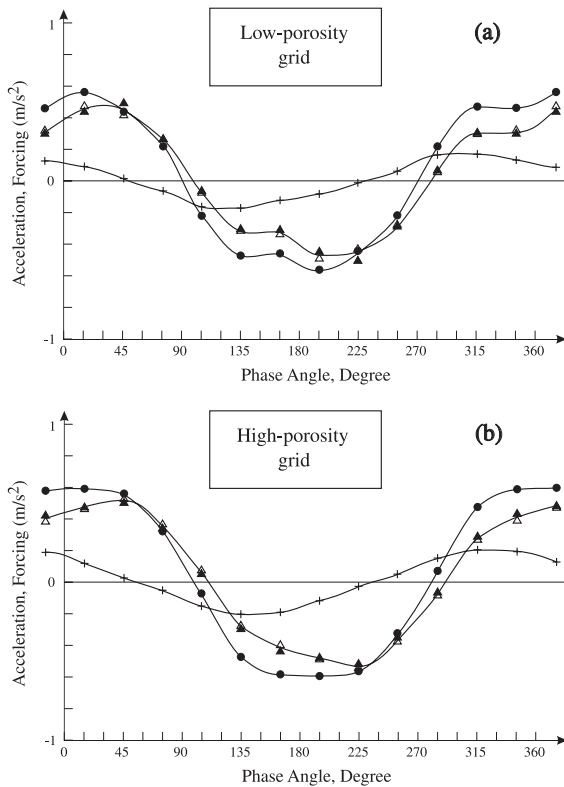


Fig. 19. Time variation of the terms in the horizontal force balance. Circles: the acceleration term. Crosses: the Reynolds stress term. Triangles: the pressure-gradient term (empty triangles: the thickness of the near-bed layer is $0.02a$; filled triangles: the thickness of the near-bed layer is $0.06a$).

every second half cycle, as the surface roller passes the location considered, and the associated shear stress is in on direction only, corresponding to an onshore directed surface shear stress. The magnitude of the time averaged near-surface shear stress in a surf zone can be estimated from the energy dissipation in the breaking/broken waves, see e.g. Fredsøe and Deigaard (1992). It is found that the estimated vertical gradient in the mean shear stress in a surf zone is significantly smaller (about a factor 5) than the maximum vertical gradient in the Reynolds shear stress found in the present experiments. Even though the shear stress in a surf zone may vary through a wave period the near-bed vertical gradient is in any case expected to be smaller than in the experiment.

As a conclusion the free stream velocity (the velocity at the top of the boundary layer) is practically the same in the experiment with and without grids. In order to attain this outer velocity in the grid experiments the horizontal pressure gradient is modified (mainly in the form of a phase shift) to balance the shear stresses associated with the outer boundary layer formed under the grid at each half cycle. The outer boundary layer does not reach the near-bed boundary layer until after the peak in the outer flow velocity, and the influence of the outer shear stress on the near-bed boundary layer during its formation in the acceleration phase is expected to be small.

5.2. Inner-flow representation

Another way of plotting the results is to use the inner-flow parameters, which gives a better picture of the boundary layer behavior near the bed, and furthermore relates the oscillatory boundary layer to the familiar steady boundary layers.

5.2.1. Mean velocity profiles

Fig. 20 compares the mean velocity profiles at $\omega t = 90^\circ$ for the grid experiments with the corres-

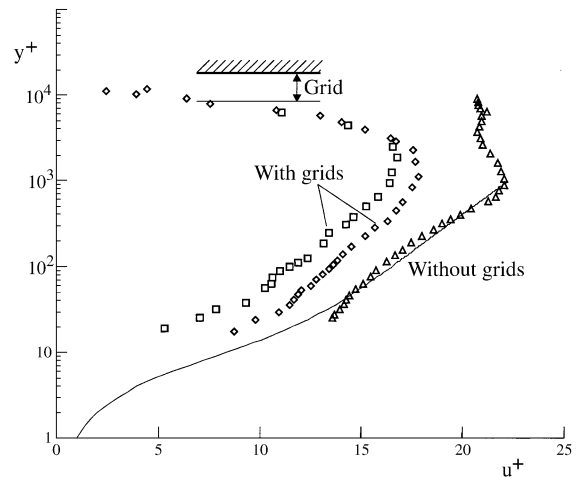


Fig. 20. Velocity profiles at $\omega t = 90^\circ$ plotted in inner flow parameters. Squares: low-porosity grid, Test 11, Table 1, $Re = 1.74 \times 10^6$; diamonds: high-porosity grid, Test 11, Table 2, $Re = 1.79 \times 10^6$; triangles: undisturbed case, Test 1, Table 3, $Re = 1.72 \times 10^6$. Solid line: van Driest (1956) profile (Eq. (5.4)) for $k_s^+ < 4$ (hydraulically smooth).

ponding velocity profile for the undisturbed case in terms of the inner-flow parameters. Here

$$\bar{u}^+ = \frac{\bar{u}}{U_f} \quad (5.2)$$

and

$$y^+ = \frac{yU_f}{\nu} \quad (5.3)$$

in which U_f is the bed shear velocity at $\omega t = 90^\circ$. Note that the directly measured values of U_f are used in the plotting. In the figure, the van Driest (1956) profile for the case of a hydraulically smooth wall is also plotted:

$$\bar{u}^+ = 2 \int_0^{y^+} \frac{dy^+}{1 + \{1 + 4\kappa^2 y^{+2} [1 - \exp(-y^+/A)]^2\}^{\frac{1}{2}}} \quad (5.4)$$

Here, κ is the von Karman constant ($\kappa = 0.4$) and A is the van Driest damping factor, where, $A = 25$ (\bar{u}^+ tends to the logarithmic distribution $\bar{u}^+ = (1/\kappa) \ln y^+ + 5$ for large y^+ values, the straight line portion of the curve).

Fig. 20 clearly shows that the present grid-case velocity profiles are displaced upwards, and they cannot be represented by the smooth-wall van Driest profile.

The effect of the externally generated turbulence on the velocity profiles may be parameterized by introducing an “apparent roughness” in the formulation of the van Driest velocity profile. To determine the value of this apparent roughness for the measured velocity profiles, the rough-wall form of the van Driest profile:

$$\bar{u}^+ = 2 \int_0^{y^+} \frac{dy^+}{1 + \{1 + 4\kappa^2 (y + \Delta y^+)^2 [1 - \exp(-(y + \Delta y^+)/A)]^2\}^{\frac{1}{2}}} \quad (5.5)$$

is fitted to the measured velocity profiles. Here Δy^+ , the coordinate shift, is given as:

$$\Delta y^+ = 0.9 [\sqrt{k_s^+} - k_s^+ \exp(-k_s^+/6)] \quad (5.6)$$

in which k_s^+ is the normalized Nikuradse equivalent sand roughness:

$$k_s^+ = \frac{k_s U_f}{\nu} \quad (5.7)$$

(Rotta, 1962; Cebeci and Chang, 1978). This exercise gives an apparent roughness of $k_s^+ = 20$ and 40 for the high-porosity and low-porosity grids, respectively. Fig. 21 displays the measured velocity profiles together with the van Driest rough-wall profiles for $k_s^+ = 20$ and 40. Note that the van Driest rough-wall profile tends to the familiar logarithmic distribution $\bar{u}^+ = (1/\kappa) \ln(30y/k_s)$ for large distances from the bed. In the aforementioned exercise, the coordinate shift (Eq. (5.6)) is found to be $\Delta y^+ = 5.6$ and 3.4 for the low-porosity and high-porosity grids, respectively. (In the plot of the measured velocity profiles in Fig. 21, the respective Δy^+ values were added to the actual y coordinates measured from the bed. This small coordinate shift makes, however, practically no change in the calculation of k_s^+).

The preceding result, namely, the existence of an “apparent roughness”, in the presence of externally generated turbulence, is consistent with the finding that the friction coefficient increases with the presence of the grid (Fig. 11).

It may be appropriate at this point to include some discussion related to the previous interpretation of the results in terms of an “apparent roughness”. There are analogies between the conditions in the present experi-

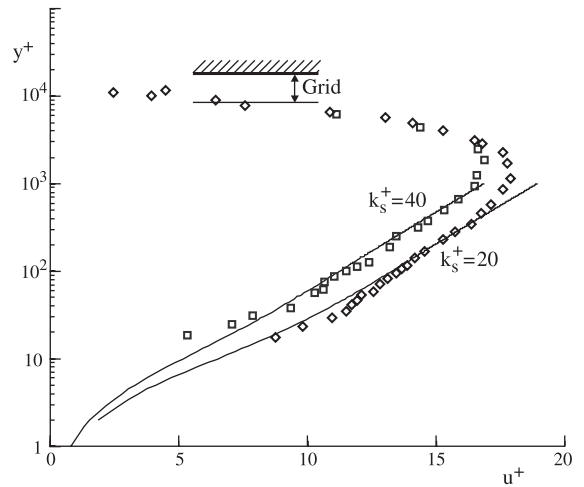


Fig. 21. Velocity profiles at $\omega t = 90^\circ$ plotted in inner flow parameters. Squares: low-porosity grid, Test 11, Table 1, $Re = 1.74 \times 10^6$; diamonds: high-porosity grid, Test 11, Table 2, $Re = 1.79 \times 10^6$. Solid lines: van Driest (1956) profile (Eq. (5.5)) for $k_s^+ = 20$ and 40, for high-porosity and low-porosity grids, respectively.

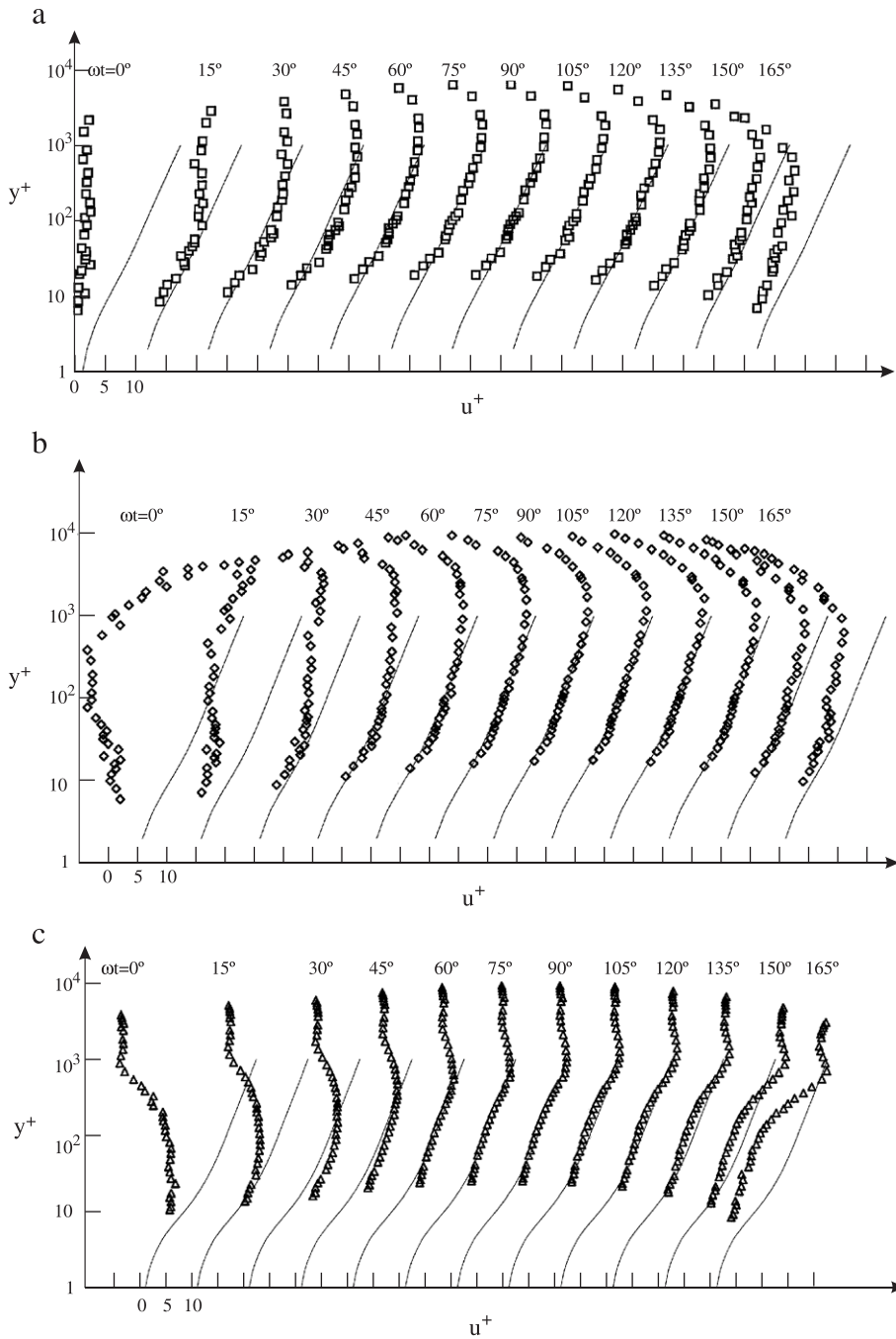


Fig. 22. (a) Mean velocity distributions, in semi-logarithmic plot: low-porosity grid, Test 11, Table 1, $Re = 1.74 \times 10^6$. Solid line: van Driest (1956) profile (Eq. (5.5)) for $k_s^+ = 40$. (b) Mean velocity distributions, in semi-logarithmic plot: high-porosity grid, Test 11, Table 2, $Re = 1.79 \times 10^6$. Solid line: van Driest (1956) profile (Eq. (5.5)) for $k_s^+ = 20$. (c) Mean velocity distributions, in semi-logarithmic plot: undisturbed case, Test 2, Table 3, $Re = 1.72 \times 10^6$. Solid line: van Driest (1956) profile (Eq. (5.4)).

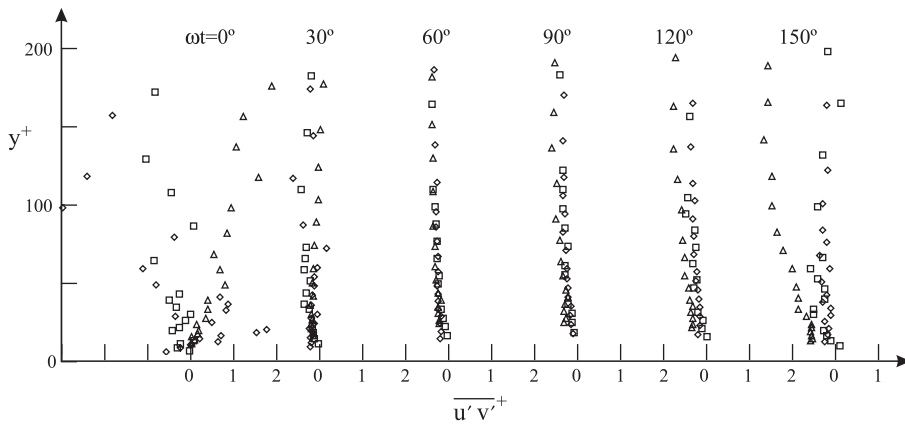


Fig. 23. Distribution of $\overline{u'v'}$ in inner flow parameters. Squares: low-porosity grid, Test 11, Table 1, $Re=1.74 \times 10^6$; diamonds: high-porosity grid, Test 11, Table 2, $Re=1.79 \times 10^6$; triangles: undisturbed case, Test 1, Table 3, $Re=1.72 \times 10^6$.

ments and the interaction between a turbulent oscillatory boundary layer and a steady current. Due to the nonlinearity in the relation between the near-bed flow velocity and the bed shear stress in a turbulent boundary layer the time averaged bed shear stress is increased when an oscillatory motion is added to the mean current (provided that the oscillatory flow is in the turbulent regime and the combined flow is in the “wave-dominated” regime, Lodahl et al., 1998). This has been quantified as an increased flow resistance for the mean current and may be expressed by an apparent ‘wave roughness’ that determines the character of the mean current velocity distribution outside the oscillatory boundary layer. Quantitative models for the com-

bined wave–current boundary layer have until now only been presented for a rough bed condition (e.g. Grant and Madsen, 1979; Fredsøe, 1984) but, for a smooth bed, the flow resistance for the mean current could just as well be expressed as an apparent wave roughness. This is a way of quantifying the effect of the wave–current interaction, and does not imply that the actual instantaneous flow conditions at the bed deviates from a hydraulically smooth wall.

In the present experiments, the oscillatory flow interacts with the externally generated turbulence with a time scale much shorter than the oscillation period. In an analogy with the wave–current boundary layer the present oscillatory motion corresponds thus to the

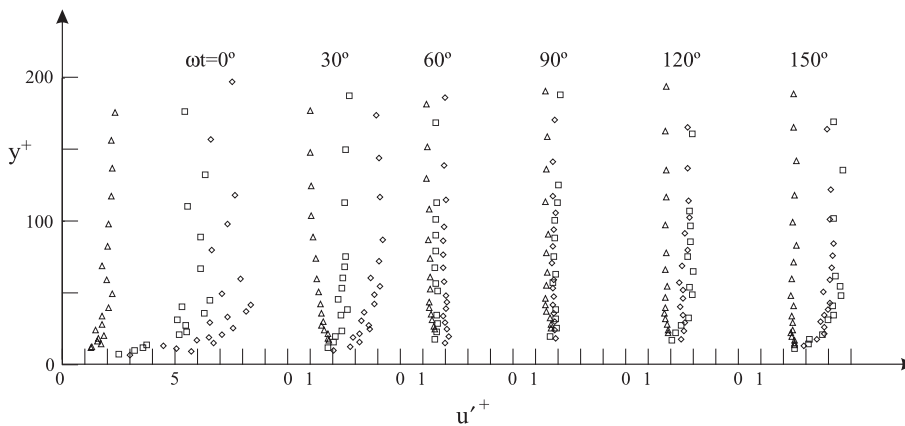


Fig. 24. Distribution of $\sqrt{u'^2}$ in inner flow parameters. Squares: low-porosity grid, Test 11, Table 1, $Re=1.74 \times 10^6$; diamonds: high-porosity grid, Test 11, Table 2, $Re=1.79 \times 10^6$; triangles: undisturbed case, Test 1, Table 3, $Re=1.72 \times 10^6$.

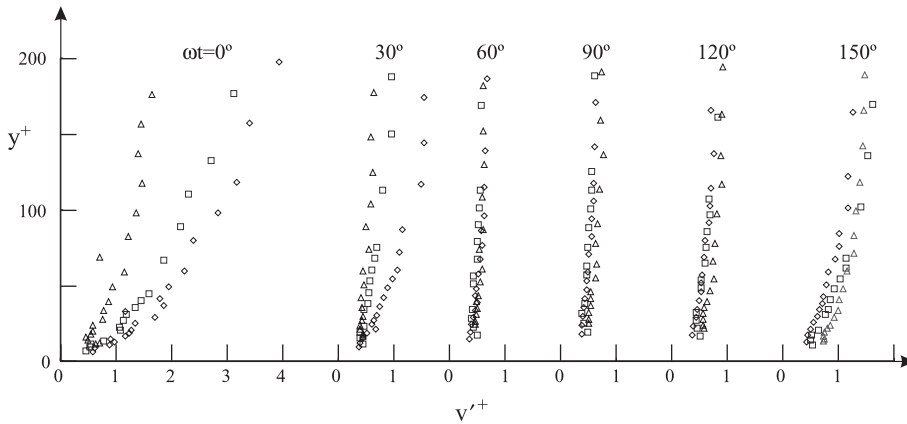


Fig. 25. Distribution of $\sqrt{v'^2}$ in inner flow parameters. Squares: low-porosity grid, Test 11, Table 1, $Re = 1.74 \times 10^6$; diamonds: high-porosity grid, Test 11, Table 2, $Re = 1.79 \times 10^6$; triangles: undisturbed case, Test 1, Table 3, $Re = 1.72 \times 10^6$.

steady current while the external turbulence plays the role of the wave induced motion. The effect of the turbulence on the oscillatory boundary layer is therefore quantified in the above analysis as an “apparent roughness” parameter.

Fig. 22a–c presents the velocity profiles plotted in terms of the inner-flow parameters at successive phase values over one-half period of motion for the low-porosity grid, high-porosity grid and undisturbed-flow cases, respectively. The directly measured, temporal values of U_f are used to normalize the quantities \bar{u} and y . The rough-wall van Driest profiles for $k_s^+ = 40$ and 20 (Fig. 21), together with the smooth wall van Driest profile are retained in Fig. 22a–c, respectively, as a reference line, for all the phase values. The figures show that the logarithmic layer, the straight line portion of the velocity profile, first emerges when $\omega t \sim 15$ –

30°, and subsequently grows in thickness, similar to the observations made by Jensen et al. (1989, Fig. 15) for a normal boundary layer flow. The only difference between the present grid results and that of Jensen et al.’s (1989) is that, in the present case, the logarithmic profile is shifted, which can be parameterized by introducing an apparent roughness, as described above.

5.2.2. Fluctuating velocity profiles

Figs. 23–25 present the turbulence quantities, $\frac{u'v'}{u'v'}$, $\sqrt{u'^2}$ and $\sqrt{v'^2}$ in terms of the inner-flow parameters. It is interesting to note that the data for all the turbulence quantities in the phase interval $60^\circ \leq \omega t \leq 120^\circ$ practically collapse although the undisturbed $\sqrt{u'^2}$ appears to be slightly smaller than that in the grid case. This may indicate that, for these phase values, the process of turbulent momentum exchange

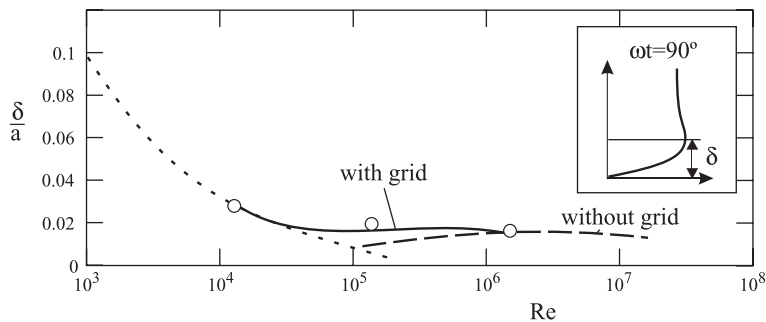


Fig. 26. Boundary layer thickness. Circles: low-porosity grid; dashed line: from Jensen et al. (1989); and dotted line: laminar flow solution (Eq. (5.8)).

in the boundary layer, in the case of the grids, occurs in much the same way in the case of the undisturbed boundary layer.

5.3. Boundary layer thickness

The nondimensional bed boundary layer thickness, δ/a , for the present low-porosity grid case is presented in Fig. 26 as a function of Re . The definition of δ is included in the figure. The laminar boundary layer solution (Batchelor, 1967)

$$\frac{\delta}{a} = \frac{3\pi}{4} \left(\frac{2}{Re} \right)^{\frac{1}{2}} \tag{5.8}$$

is presented as well. The boundary layer thickness for the high-porosity grid is similar to the low-porosity grid case. The boundary layer thickness is apparently larger in the present case than in the case without the grids, at moderate Reynolds numbers ($7 \times 10^4 \lesssim Re \lesssim 1 \times 10^6$). This is linked with the early transition to turbulence in the bed boundary layer, at $Re = 7 \times 10^4$.

6. Autocorrelation and macro-time scales

The autocorrelation coefficient is defined by:

$$R_{xx}(y, \tau) = \frac{\langle u'(y, t)u'(y, t + \tau) \rangle}{\langle u'^2(y) \rangle} \tag{6.1}$$

where u' is the fluctuating component of the velocity, $u' = u - \bar{u}$, and \bar{u} is the ensemble average defined by

Eq. (3.2). In the preceding equation, τ is the time lag and the brackets, $\langle \rangle$, indicate time averaged quantities over a phase interval of 45° . The phase interval was chosen after a sensitivity study showed that convergence of the results was achieved for a phase interval of 40° .

A typical result obtained for the high-porosity grid case is shown in Fig. 27, at $\omega t = 90^\circ$ calculated over the 45° phase interval of $67.5^\circ < \omega t < 112.5^\circ$. Also included in the figure is a typical result for the undisturbed case.

The macro-time scale, T_x , is defined by

$$T_x(y) = \int_0^{t_0} R_{xx}(y, \tau) d\tau \tag{6.2}$$

where t_0 corresponds to the first zero crossing of the autocorrelation function (Fig. 27). The first zero crossing was chosen rather than ∞ for the upper bound of the above integral because of the uncertainty in the value of R_{xx} for large values of time. Recall that the entire length of the phase interval over which the correlation is calculated is only 45° . See further discussion in the following paragraphs.

As mentioned earlier, five cycles were sampled for the autocorrelation measurements (Tables 1–3). A mean value of the macro-time scale is calculated by

$$\bar{T}_x(y) = \frac{1}{n} \sum_{i=1}^n T_x(y) \tag{6.3}$$

in which n in the present case is 10 (corresponding to the five sampled wave cycles).

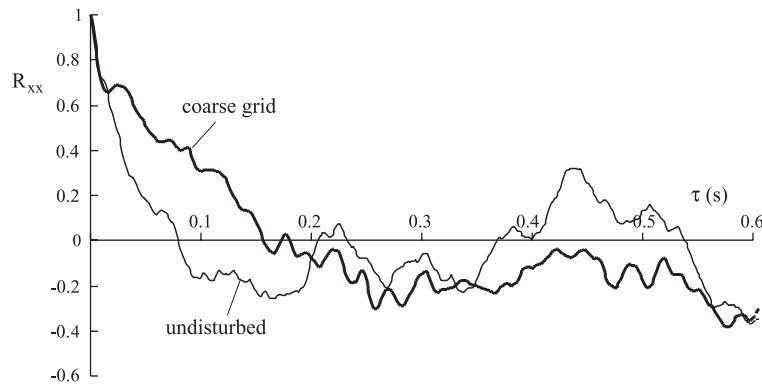


Fig. 27. The autocorrelation function calculated for a typical half cycle of motion, at $\omega t = 90^\circ$, for velocity measurements taken at $y = 6.5$ cm; high-porosity grid: Test 14, Table 2, $Re = 1.79 \times 10^6$; and the undisturbed case, Test 2, Table 3, $Re = 1.72 \times 10^6$.

Fig. 28 presents a comparison of the time scales for the high-porosity grid case and the present undisturbed case. The standard deviations, σ_T , corresponding to the statistics are also depicted in the figure. The large value of σ_T is due to the finite sample size ($n=10$). Unfortunately, larger number of cycles in the correlation measurements proved difficult due to the very small sampling interval used in the experiments, which was necessary for sufficient resolution of the autocorrelation function. Nevertheless, despite the large values of σ_T , the sample size used in the experiments is deemed

sufficient to obtain significantly different results, from the two cases tested (see Fig. 28).

First of all, the macro-length scales for the undisturbed case, determined from $l_x = \bar{u}T_x$ and $l_y = \bar{u}T_y$, compare favorably with the result obtained from $l = \kappa y$. (The latter relationship, known from the steady boundary layer research, has been revealed from Sumer et al., 1987 for an oscillatory boundary layer.)

Secondly, the time scales obtained, with the grid, is presumably attributed to vortices generated by the grids.

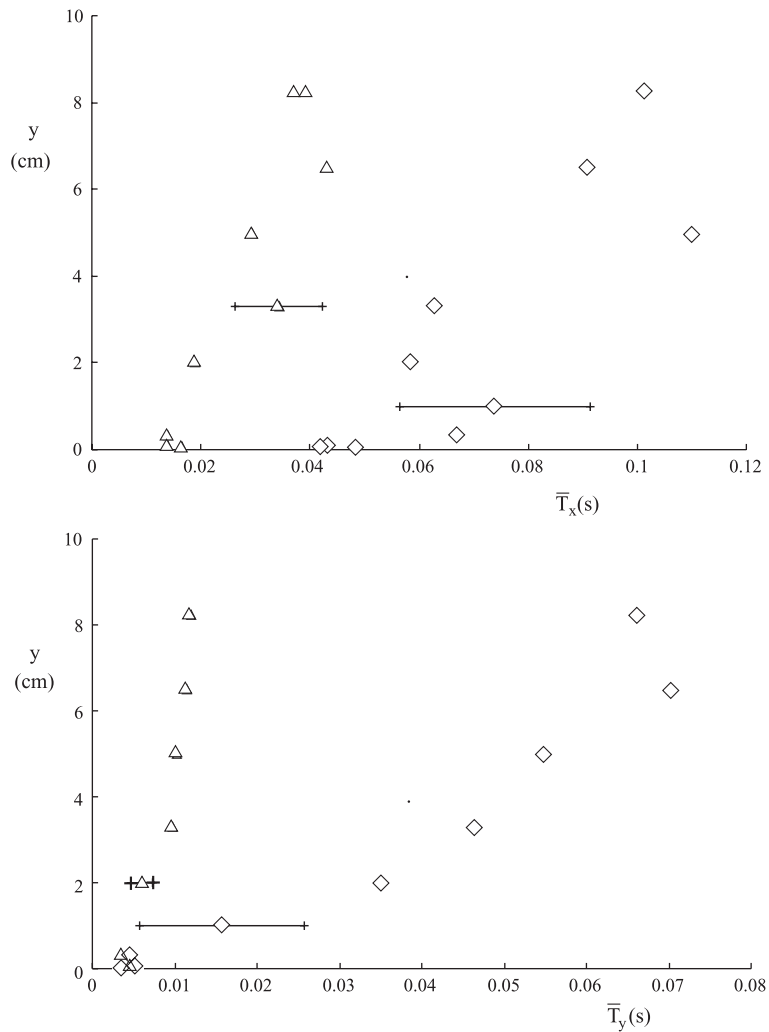


Fig. 28. Comparison of macro-time scales. Diamonds: high-porosity grid, Test 14, Table 2, $Re = 1.79 \times 10^6$; triangles: undisturbed case, Test 2, Table 3, $Re = 1.72 \times 10^6$.

Thirdly, it is seen from Fig. 28 that the time scale increases with increasing distance from the bed, as expected.

The autocorrelation and time scale measurements have also been made for the low-porosity grid, for a few cases. (Basically, these measurements were not included in the original experimental program.) Nevertheless, these limited measurements show that the time scales obtained for the low-porosity grid are a factor of 2 larger than that for the high-porosity grid. This may be attributed to the smaller velocities experienced in the grid region in the case of the low-porosity grid, meaning that T_v should, in this case, be larger.

6.1. Discussion

The near-bed conditions for the turbulence in a surf zone corresponds in many respect to a shear free boundary layer where externally generated homogeneous turbulence interacts with a solid wall (Deigaard et al., 1991). Shear free boundary layers (SFBL) have received considerable attention during the last 30 years in experimental, theoretical and numerical investigations. Some of the important references are: Thomas and Hancock (1977), Uzkan and Reynolds (1967), Hunt and Graham (1978), Hunt (1984), Biringen and Reynolds (1981), Perot and Moin (1995), Aronson et al. (1997).

A conceptually simple model based on rapid distortion theory was introduced by Hunt and Graham (1978) and further discussed by Hunt (1984). This model represents the characteristics of the turbulence in an SFBL in many respects. The principle of the rapid distortion model is to obtain a zero velocity normal to the wall (by introducing a potential flow field that cancels out the wall-normal velocity fluctuations at the wall). The total flow field is thus a superposition of the homogeneous turbulence with an irrotational velocity field driven by a distribution of sources at the bed, which cancels the vertical velocity fluctuations there. This source field decays away from the wall over a length scale of the order L_0 , the integral length scale of the turbulence away from the wall. The wall normal velocity fluctuations thus gradually decay to zero at the wall over this layer with a thickness scaled by L_0 . The deflection of the flow towards the wall causes a gradual increase in the

turbulent velocity fluctuations parallel to the wall. In the case of isotropic turbulence away from the wall the rapid distortion theory predicts that the mean-square value of a wall-parallel velocity fluctuation increases gradually to 1.5 times the mean-square value of it away from the wall.

Due to the nonslip boundary condition at the wall unsteady boundary layers are formed when the turbulent eddies “scrape” along the wall, these boundary layers can be laminar or—in the case of a very large Reynolds number of the free stream turbulence—they may become turbulent.

If a mean boundary layer flow is formed along the bed, turbulence is generated in the boundary layer in addition to the free stream turbulence. Hunt (1984) argues that there is statistical independence between the turbulence generated in the shear flow along the wall and the externally generated turbulence, which varies through the source layer.

As described earlier the free stream turbulence in the present experiments formed partly by the flow through the grid and partly in the shear layer beneath it. The free stream turbulence is therefore not isotropic. It is still relevant to interpret and compare some of the results in the present experiments with the predictions by the rapid distortion theory, particularly since the conditions in an SFBL may be representative for the near-bed conditions in a surf zone.

The magnitude of the integral length scale can be inferred from the macro-time scale (Fig. 28). Away from the bed, the transverse macro-time scales are about 0.06–0.07 s, the time scales are determined over phase interval of 45° around the peak velocity at 90° , and with a free stream velocity amplitude of 1.09 m/s; the transverse free stream length scale, ℓ_{y0} , is estimated to be about 0.07 m.

In Fig. 28, the transverse time scale (and therefore also length scale) with the grid present is seen to decrease almost linearly towards a value close to zero at the bed. The decrease occurs over a height approximately equal to ℓ_{y0} , in agreement with the prediction of the rapid distortion model of Hunt and Graham (1978).

The vertical velocity fluctuations with the grid present decreases towards zero at the bed (Fig. 16); the decrease is more pronounced within the distance ℓ_{y0} ($y/a \sim 0.04$) from the bed as would be expected from the model. Quantitative comparison with the

model results is difficult due to the combined effect of decay of the grid generated turbulence with the distance from the grid, the turbulence generated in the near-bed oscillatory boundary layer with a thickness less than ℓ_{y0} and the decrease of the grid generated turbulence due to the proximity to the bed.

The characteristics of the longitudinal time and length scales and the horizontal velocity fluctuations are less clear. With the grid present the horizontal velocity fluctuations (cf. Fig. 15) increase toward the bed as would be expected from the rapid distortion theory, but the increase is not more pronounced than found without the grid due to the production of turbulence in the oscillatory boundary layer. The longitudinal length scale, Fig. 28, does show decrease towards the bed as expected from the rapid distortion theory of Hunt and Graham (1978). As in the experiments of Brumley and Jirka (1987), who studied turbulence near a free surface, the quantitative agreement for the longitudinal length scale is less good than for the vertical.

7. Conclusions

1. The level of turbulence, throughout the entire depth of the oscillator, was substantially increased as a result of the introduction of the grids. The externally generated turbulence penetrated the bed boundary layer, giving rise to an increase in both the mean and r.m.s. values of the bed shear stress, when compared to the undisturbed case.
2. The critical Reynolds number where transition-to-turbulence occurs reduces as the level of turbulence in the flow is increased. This is in accordance with results obtained from steady, boundary layer flow research. The onset of transition is accompanied by the appearance of spikes in the bed shear stress measurements, just prior to flow reversals, similar to that observed in previous studies for the undisturbed case.
3. Other features, such as: (i) the change in phase of the mean bed shear stress with changing Re ; and (ii) the spreading of turbulence (the r.m.s. value of the bed shear stress fluctuations) towards smaller phase values, with increasing Re are also observed.
4. The friction coefficient increases with the increase in turbulence in the flow.
5. The enhancement in the momentum exchange between the bed and outer flow results in a reduction of the phase lead of the bed shear stress over the velocity at the outer edge of the bed boundary layer.

Acknowledgements

This study was partially funded by the Commission of the European Communities, Directorate-General XII for Science, Research and Development Program Marine Science and Technology (MAST III) Contract No. MAS3-CT97-0081 “Surf and Swash Zone Mechanics” (SASME), FP5 EESD Programme Contract No. EVK3-2000-00037 “Human Interaction with Large Scale Coastal Morphological Evolution” (HUMOR) and by the Danish Technical Research Council (STVF) research project “Coast and Tidal Inlets”.

Dr. N.-S. Cheng of Nanyang Technological University conducted some of the tests reported in the paper.

References

- Aronson, D., Johansson, A.V., Lofdahl, L., 1997. Shear free turbulence near a wall. *J. Fluid Mech.* 338, 363–385.
- Batchelor, G.K., 1967. *An Introduction to Fluid Dynamics*. Cambridge Univ. Press.
- Biringen, S., Reynolds, W.C., 1981. Large eddy simulation of the shear-free turbulent boundary layer. *J. Fluid Mech.* 103, 53–63.
- Brumley, B.H., Jirka, G.H., 1987. Near-surface turbulence in a grid-stirred tank. *J. Fluid Mech.* 183, 235–264.
- Cebeci, T., Chang, K.C., 1978. Calculations of incompressible rough-wall boundary layer flows. *AIAA J.* 16, 730.
- Deigaard, R., Justesen, P., Fredsøe, J., 1991. Modelling of undertow by a one-equation turbulence model. *Coast. Eng.* 15, 431–458.
- Fedderson, F., Guza, R.T., 2000. Velocity moments in alongshore bottom stress parameterizations. *J. Geophys. Res.* 105 (C4), 8673–8686.
- Fedderson, F., Guza, R.T., Elgar, S., Herbers, T.H.C., 1998. Alongshore momentum balances in the nearshore. *J. Geophys. Res.* 103 (C8), 15667–15676.
- Fredsøe, J., 1984. Turbulent boundary layer in wave–current motion. *J. Hydraul. Eng.* 110 (8), 1103–1120.
- Fredsøe, J., Deigaard, R., 1992. *Mechanics of Coastal Sediment Transport*. Advanced Series on Ocean Engineering, vol. 3. World Scientific.
- Grant, W.D., Madsen, O.S., 1979. Combined wave and current interaction with a rough bottom. *J. Geophys. Res.* 84 (C4), 1797–1808.

- Grant, W.D., Madsen, O.S., 1986. The continental-shelf bottom boundary layer. *Annu. Rev. Fluid Mech.* 18, 265–305.
- Hino, M., Sawamoto, M., Takasu, S., 1976. Experiments on transition to turbulence in an oscillatory pipe flow. *J. Fluid Mech.* 75, 193–207.
- Hino, M., Kashiwayanagi, M., Nakayama, A., Hara, T., 1983. Experiments on the turbulence statistics and the structure of a reciprocating oscillatory flow. *J. Fluid Mech.* 131, 363–400.
- Hunt, J.C.R., 1984. Turbulence structure in thermal convection and shear free boundary layers. *J. Fluid Mech.* 138, 161–184.
- Hunt, J.C.R., Graham, J.M.R., 1978. Free-stream turbulence near plane boundaries. *J. Fluid Mech.* 84, 209–235.
- Jensen, B.L., Sumer, B.M., Fredsøe, J., 1989. Turbulent oscillatory boundary layers at high Reynolds numbers. *J. Fluid Mech.* 206, 265–297.
- Lodahl, C.R., Sumer, B.M., Fredsøe, J., 1998. Turbulent combined oscillatory flow and current in a pipe. *J. Fluid Mech.* 373, 313–348.
- Lundgren, H., Sørensen, T., 1958. A pulsating water tunnel. *Proc. 6th Int. Conf. on Coastal Engineering*, Miami, FL. Council on Wave Research, The Eng. Foundation, Engineering Field Station, University of California, Richmond, CA, pp. 356–358.
- Peregrine, D.H., Svendsen, I.A., 1978. Spilling breakers, bores and hydraulic jumps. *Proc. 16th Int. Conf. on Coastal Engineering*, ASCE, Hamburg, pp. 540–550.
- Perot, B., Moin, B., 1995. Shear free turbulent boundary layers: Part 1. Physical insight into near-wall turbulence. *J. Fluid Mech.* 295, 199–227.
- Ribberink, J.S., Alselaam, A.A., 1995. Sheet flow and suspension of sand in oscillatory boundary layers. *Coast. Eng.* 25 (3–4), 205–225.
- Rotta, J.C., 1962. Turbulent boundary layers in incompressible flow. *Prog. Aerosp. Sci.* 2 (1).
- Schlichting, H., 1979. *Boundary Layer Theory*. McGraw-Hill Book.
- Sumer, B.M., Jensen, B.L., Fredsøe, J., 1987. Turbulence in oscillatory boundary layers. *Advances in Turbulence. Proc. 1st European Conference*. Springer, Lyon, France, pp. 556–567.
- Sumer, B.M., Arnskov, M.M., Christiansen, N., Jørgensen, F.E., 1993. 2-Component hot-film probe for measurement of wall shear stress. *Exp. Fluids* 15 (6), 380–384.
- Thomas, N.H., Hancock, P.E., 1977. Grid turbulence near a moving wall. *J. Fluid Mech.* 82, 481–496.
- Uzkan, T., Reynolds, W.C., 1967. A shear-free turbulent boundary layer. *J. Fluid Mech.* 28, 803–821.
- van Driest, E.R., 1956. On turbulent flow near a wall. *J. Aerosp. Sci.* 23, 1007–1011.